

Correlated quantum dynamics of two quenched fermionic impurities immersed in a Bose-Einstein Condensate

S. I. Mistakidis,¹ L. Hilbig,¹ and P. Schmelcher^{1,2}

¹*Center for Optical Quantum Technologies, Department of Physics, University of Hamburg, Luruper Chaussee 149, 22761 Hamburg Germany*

²*The Hamburg Centre for Ultrafast Imaging, Universität Hamburg, Luruper Chaussee 149, 22761 Hamburg, Germany*

(Dated: August 28, 2019)

We unravel the nonequilibrium dynamics of two fermionic impurities immersed in a one-dimensional bosonic gas following an interspecies interaction quench. Monitoring the temporal evolution of the single-particle density of each species we reveal the existence of four distinct dynamical regimes. For weak interspecies repulsions both species either perform a breathing motion or the impurity density splits into two parts which interact and disperse within the bosonic cloud. Turning to strong interactions we observe the formation of dark-bright states within the mean-field approximation. However, the correlated dynamics shows that the fermionic density splits into two repelling density peaks which either travel towards the edges of the bosonic cloud where they equilibrate or they approach an almost steady state propagating robustly within the bosonic gas which forms density dips at the same location. For these strong interspecies interactions an energy transfer process from the impurities to their environment occurs at the many-body level, while a periodic energy exchange from the bright states (impurities) to the bosonic species is identified in the absence of correlations. Finally, inspecting the one-body coherence function for strong interactions enables us to conclude on the spatial localization of the quench-induced fermionic density humps.

I. INTRODUCTION

Ultracold atoms offer a fertile testbed to monitor the nonequilibrium dynamics of quantum many-body (MB) systems due to their extraordinary degree of control. Recent experimental progress enables us, for instance, to adjust the interparticle interaction strength via Feshbach resonances [1, 2], and also realize multicomponent quantum gases consisting either of different isotopes [3] or different hyperfine states [4, 5] of the same species. Multicomponent quantum systems characterized by high population imbalanced components [6–17] have been a focal point of studies examining in particular the dressing of mobile impurities with the collective excitations of a surrounding MB system forming quasiparticles often referred to as polarons. As a consequence of this dressing mechanism a variety of the impurities properties, such as their effective mass and induced interactions can be strongly altered compared to the bare particle case. Beyond ultracold atoms applications include a multitude of different systems such as semiconductors [18], high temperature superconductors [19], doped Mott insulators [20] and liquid Helium mixtures [21, 22].

The study of a mobile impurity immersed in an ultracold quantum gas has already provided numerous insights regarding Fermi [23–36] and more recently Bose polarons [37–48]. The majority of the theoretical investigations have focused on the stationary properties of these quasiparticle states and have been restricted to the mean-field (MF) approximation [49–52] and to the Fröhlich model [53–58]. Moreover, experimental evidences on the existence and dynamics of Fermi [12, 13, 16] and Bose [39, 40, 59–62] polarons have triggered a new era of theoretical investigations in order to understand

their nonequilibrium dynamics evincing also the necessity of taking into account higher-order correlations for an adequate description of the observed dynamics. Indeed, the impurities constitute a few-body system and correlation effects are expected to be well-pronounced. In this direction theoretical approaches that include correlations have been recently applied both to the Fermi [63] and mainly to the Bose polaron problem [64–74], thereby enabling a first description of these quasiparticles also in the intermediate and strong interaction regime.

Despite the above-mentioned increasing amount of theoretical and experimental efforts, the nonequilibrium dynamics of such impurity systems is still largely unexplored. Especially in the case where more than a single impurity atom is involved and thus their interactions come into play. The simplest setup in order to advance our understanding of the emerging dynamics and reveal the correlation effects consists of two fermions immersed in a MB bosonic gas. In this case, the constituting particles obey different statistics [75, 76] and the impurities are non-interacting allowing us to avoid the additional complexity introduced by the intraspecies interactions. For this scenario, it would be particularly interesting to explore the dynamical response of the impurities for distinct interspecies interaction strengths and unveil the correlation properties of the quench-induced states. These might include the emergence of an orthogonality catastrophe for strong interactions [77], the formation of dark-bright (DB) soliton complexes [78, 79] or phase separation phenomena [80, 81]. To this end, we study the interspecies interaction quench dynamics of such a harmonically trapped Bose-Fermi (BF) mixture, both within a MF and a MB treatment, from weak to strong repulsions. To track the correlated quantum dynamics of the BF

mixture we employ the Multi-Layer Multi-Configuration Time-Dependent Hartree Method for Atomic Mixtures (ML-MCTDHX) [82], which is a non-perturbative variational method capturing all interparticle correlations.

Regarding the ground state properties of the system we show that a phase separation process between the two species occurs, both at the MF and the MB level, for interspecies interaction strengths larger than the bosonic intraspecies ones [83–86]. To induce the dynamics we apply an interspecies interaction quench starting from a weakly repulsive ground state. Depending on the postquench interspecies coupling we realize four different dynamical regimes. For weak postquench interactions both species remain miscible and perform a breathing motion [86, 87]. Increasing the postquench interaction strength the single-particle density of the impurities splits into two effectively repelling density peaks that are seen to disperse within the bosonic gas. This behavior is more pronounced at the MB level. In the strong interspecies interaction regime and focusing on the MF approximation we observe the spontaneous generation of two DB solitary waves, with the bright solitons emerging in the fermionic species and the dark ones appearing in the bosonic gas. These structures interact repelling and approaching one another throughout evolution. In sharp contrast, in the MB description these solitary waves soon after their formation are pushed towards the edges of the bosonic gas remaining there in the course of the evolution, exhibiting also a gradually decaying amplitude. Entering the very strong interspecies interaction regime we again observe the formation of DB structures in both approaches. In contrast to their MF evolution, the DB solitary waves formed at the MB level tend, for later evolution times, to approach an almost steady state. Within the latter two strongly interacting regimes it is found that an energy exchange process, from the impurities to the bosonic bath, takes place in the presence of correlations. Moreover, monitoring the one-body coherence function reveals the appearance of Mott-like correlations [80, 81, 88, 92] between the emergent bright solitary waves indicating their tendency for localization. Finally inspecting the dynamics of the fermionic two-body reduced density matrix we unveil that depending on the postquench interaction strength the two fermionic impurities either behave almost independently or experience a weak attraction for very strong interspecies couplings.

The present work is structured as follows. Section II presents our setup and the different observables that are used for the identification of the correlated character of the observed dynamics. The nonequilibrium dynamics induced by an interspecies interaction quench of the particle imbalanced BF mixture is discussed in Sec. III. We summarize and provide an outlook in Section IV. Finally, in Appendix A we provide further details of our numerical simulations and demonstrate their convergence exemplarily.

II. THEORETICAL FRAMEWORK

A. Setup

We consider a particle imbalanced BF mixture consisting of $N_F = 2$ spin polarized fermionic impurities and $N_B = 100$ bosons which constitute the majority species. The mixture is further assumed to be mass balanced, namely $M_B = M_F \equiv M$, while each species is trapped in the same external harmonic oscillator potential of frequency $\omega_B = \omega_F = \omega$. Such an approximately mass balanced mixture can be experimentally realized by considering e.g. a mixture of isotopes of ${}^7\text{Li}$ and ${}^6\text{Li}$ [93] or ${}^{171}\text{Yb}$ and ${}^{172}\text{Yb}$ [94, 95]. The resulting MB Hamiltonian of the system reads

$$H = \sum_{\sigma=F,B} \sum_{i=1}^{N_\sigma} \left[-\frac{\hbar^2}{2M} \left(\frac{d}{dx_i^\sigma} \right)^2 + \frac{1}{2} M \omega (x_i^\sigma)^2 \right] + g_{BB} \sum_{i < j} \delta(x_i^B - x_j^B) + g_{BF} \sum_{i=1}^{N_F} \sum_{j=1}^{N_B} \delta(x_i^F - x_j^B). \quad (1)$$

We operate within the ultracold regime and therefore s -wave scattering is the dominant interaction process. Consequently both the inter- and intraspecies interactions are described by contact interactions whose effective one-dimensional coupling strength [96] is $g_{\sigma\sigma'} = \frac{2\hbar^2 a_{\sigma\sigma'}^s}{\mu a_\perp^2} (1 - |\zeta(1/2)| a_{\sigma\sigma'}^s / \sqrt{2} a_\perp)^{-1}$. Here, $\sigma, \sigma' = B, F$ for bosons or fermions respectively and $\mu = \frac{M}{2}$ is the corresponding reduced mass. The transversal length scale reads $a_\perp = \sqrt{\hbar/\mu\omega_\perp}$ with ω_\perp denoting the transversal confinement frequency while $a_{\sigma\sigma'}^s$ is the three-dimensional s -wave scattering length within ($\sigma = \sigma'$) or between ($\sigma \neq \sigma'$) the two distinct species. Moreover, s -wave scattering is forbidden for spin-polarized fermions [75, 76], due to the antisymmetry of the fermionic wavefunction, and thus intraspecies interactions within the fermionic species are neglected. We remark that $g_{\sigma\sigma'}$ can be experimentally tuned either via $a_{\sigma\sigma'}^s$ by means of Feshbach resonances [1, 2] or by adjusting ω_\perp via confinement-induced resonances [96].

The Hamiltonian of Eq. (1) is rescaled in units of $\hbar\omega_\perp$. As a result the corresponding length, time, and interaction strength are expressed in terms of $\sqrt{\frac{\hbar}{M\omega_\perp}}$, ω_\perp^{-1} and $\sqrt{\frac{\hbar^3\omega_\perp}{M}}$ respectively.

In the present work, we prepare our system in the ground state of the Hamiltonian (1) within the weak intra- and interspecies interaction regime, namely $g_{BB} = 0.5$ and $g_{BF} = 0.1$. Therefore the two species are miscible, i.e. their one-body densities spatially overlap. Recall that in the absence of a trap species separation takes place when $g_{BF}^2 > g_{BB}$, otherwise the two species overlap [83, 84, 97]. Another important remark here is that for sufficiently strong trapping, a scenario not considered herein, the above condition needs to be modified [97] namely g_{BF} should become substantially larger than g_{BB}

in order to overcome the implicitly miscibility favoring effect of the trap. To trigger the nonequilibrium dynamics of the BF mixture we suddenly change at $t = 0$ the interspecies interaction strength towards a larger value of repulsion, e.g. $g_{BF} = 1.5$, which favors species immiscibility and let the system evolve in time. Below, we first briefly discuss the ground state properties of the system [Sec. III A] and then analyze in detail the quench-induced dynamics [Sec. III] of the two fermionic impurities immersed in the bosonic gas.

B. Wavefunction ansatz

To calculate the stationary properties of the BF mixture and most importantly the quench-induced nonequilibrium dynamics we solve the corresponding MB Schrödinger equation utilizing ML-MCTDHX [82]. This method is based on expanding the MB wavefunction with respect to a time-dependent and variationally optimized basis which allows us to take into account both the inter- and the intraspecies correlations of the BF mixture. Accordingly, in order to incorporate interspecies correlations we expand the MB wavefunction in terms of D different species functions, $\Psi_k^\sigma(\vec{x}^\sigma; t)$, for each component. In this notation the spatial $\sigma = B, F$ -species coordinates are $\vec{x}^\sigma = (x_1^\sigma, \dots, x_{N_\sigma}^\sigma)$ and the number of the σ -species atoms is N_σ . As a result, the MB wavefunction Ψ_{MB} acquires the form of a truncated Schmidt decomposition [98] of rank D

$$\Psi_{MB}(\vec{x}^F, \vec{x}^B; t) = \sum_{k=1}^D \sqrt{\lambda_k(t)} \Psi_k^F(\vec{x}^F; t) \Psi_k^B(\vec{x}^B; t). \quad (2)$$

In the following, we shall also refer to the Schmidt coefficients $\lambda_k(t)$ as the natural species populations of the k -th species function. Moreover, the system is assumed to be entangled [99] or interspecies correlated if at least two distinct $\lambda_k(t)$ are nonzero since in this latter case Ψ_{MB} is not a direct product of two states.

Furthermore in order to include intraspecies correlations into our MB ansatz we expand each of the species functions $\Psi_k^\sigma(\vec{x}^\sigma; t)$ in terms of the determinants and permanents of d_σ distinct time-dependent fermionic and bosonic single-particle functions (SPFs) $\varphi_1^\sigma, \dots, \varphi_{d_\sigma}^\sigma$ respectively. Consequently, $\Psi_k^\sigma(\vec{x}^\sigma; t)$ is expressed as follows

$$\begin{aligned} \Psi_k^\sigma(\vec{x}^\sigma; t) &= \sum_{\substack{l_1, \dots, l_{d_\sigma} \\ \sum l_i = N}} c_{k, (l_1, \dots, l_{d_\sigma})}(t) \sum_{i=1}^{N_\sigma!} \text{sign}(\mathcal{P}_i)^\zeta \times \\ &\mathcal{P}_i \left[\prod_{j=1}^{l_1} \varphi_1^\sigma(x_j; t) \cdots \prod_{j=1}^{l_{d_\sigma}} \varphi_{d_\sigma}^\sigma(x_{K(d_\sigma)+j}; t) \right]. \end{aligned} \quad (3)$$

The index $\zeta = 0, 1$ stands for the case of bosons and fermions respectively. $\text{sign}(\mathcal{P}_i)$ refers to the sign of the

corresponding permutation with \mathcal{P} denoting the permutation operator which exchanges the particle positions x_ν^σ , $\nu = 1, \dots, N_\sigma$ within the SPFs. The symbol $K(r) \equiv \sum_{\nu=1}^{r-1} l_\nu$, where l_ν is the occupation of the ν th SPF and $r \in \{1, 2, \dots, d_\sigma\}$. Also, $c_{k, (l_1, \dots, l_{d_\sigma})}(t)$ are the time-dependent expansion coefficients of a certain determinant for fermions or permanent for bosons. Moreover, the eigenfunctions of the σ -species one-body reduced density matrix $\rho_\sigma^{(1)}(x, x'; t) = \langle \Psi_{MB}(t) | \hat{\Psi}^{\sigma\dagger}(x) \hat{\Psi}^\sigma(x') | \Psi_{MB}(t) \rangle$ are the so-called natural orbitals $\phi_i^\sigma(x; t)$. Here $\hat{\Psi}^F(x)$ and $\hat{\Psi}^B(x)$ refer to the fermionic and bosonic field operators respectively. It is worth mentioning at this point that the natural orbitals are related with the SPFs via a unitary transformation that diagonalizes $\rho_\sigma^{(1)}(x, x'; t)$ when it is expressed in the basis of SPFs, for more details see also [82, 100]. The resulting eigenvalues of $\rho_\sigma^{(1)}(x, x'; t)$ are termed natural populations $n_i^\sigma(t)$. In the following we will refer to the bosonic or fermionic subsystem as intraspecies correlated if more than one (for bosons) or N_F (for fermions) eigenvalues are macroscopically occupied. Otherwise the corresponding subsystem will be termed fully coherent or Hartree-Fock correlated respectively.

To obtain the ML-MCTDHX equations of motion [82] we follow e.g. the Dirac-Frenkel variational principle [101, 102] for the MB ansatz given by Eqs. (2), (3). This procedure results in D^2 linear differential equations of motion for the coefficients $\lambda_i(t)$ being coupled to a set of $D[\binom{N_B+d_B-1}{d_B-1} + \binom{d_F}{N_F}]$ non-linear integro-differential equations for the species functions and $d_F + d_B$ integro-differential equations for the SPFs. Another important feature of ML-MCTDHX is that it enables us to operate within different approximation orders. For instance, we can retrieve the corresponding MF equation [75, 76] of the BF mixture in the limit of $D = d_B = 1$ and $d_F = N_F$. In this latter case the MB wavefunction ansatz boils down to the following MF product state

$$\Psi_{MF}(\vec{x}^B, \vec{x}^F; t) = \frac{1}{\sqrt{N_F!}} \prod_{j=1}^{N_B} \varphi_1^B(x_j^B; t) \times \quad (4)$$

$$\sum_{i=1}^{N_F!} \text{sign}(\mathcal{P}_i) \mathcal{P}_i [\varphi_1^F(x_1^F; t) \cdots \varphi_{N_F}^F(x_{N_F}^F; t)].$$

Utilizing a variational principle, such as the Dirac-Frenkel variational principle [101, 102], we obtain the corresponding system of coupled $(N_F + 1)$ MF equations of motion [75, 79] that govern the dynamics of the BF

mixture

$$\begin{aligned}
i\frac{\partial\phi_1^B(x;t)}{\partial t} &= \left[-\frac{1}{2m}\frac{\partial^2}{\partial x^2} + \frac{1}{2}M\omega x^2 + g_{BB}N_B \right. \\
&\times \left. |\phi_1^B(x;t)|^2 + g_{BF}\sum_{i=1}^{N_F} |\phi_i^F(x;t)|^2 \right] \phi_1^B(x;t), \\
i\frac{\partial\phi_j^F(x;t)}{\partial t} &= \left[-\frac{1}{2m}\frac{\partial^2}{\partial x^2} + \frac{1}{2}M\omega x^2 \right. \\
&\left. + g_{BF}N_B \sum_{i=1}^{N_F} |\phi_i^B(x;t)|^2 \right] \phi_j^F(x;t).
\end{aligned} \tag{5}$$

Here the first equation describes the dynamics of the bosonic gas and corresponds to the well-known Gross-Pitaevskii equation of motion for a BF mixture. Moreover the equation for $\phi_j^F(x;t)$ characterizes the time-evolution of the j -th fermionic orbital and represents the set of $j = 1, \dots, N_F$ Hartree-Fock equations of motion. Within the MF approximation only the trivial Hartree-Fock intraspecies correlations are taken into account stemming from the existence of N_F distinct SPFs. A next interesting reduction of the method is the so-called species mean-field (SMF) approximation [66, 88]. Here, the entanglement between the species is ignored but the correlations within each of the species are included. Then, the total wavefunction of the system acquires the following tensor product form

$$|\Psi(t)\rangle_{SMF} = |\Psi_1^B(t)\rangle \otimes |\Psi_1^F(t)\rangle. \tag{6}$$

Indeed, the system's wavefunction is described by only one species wavefunction, i.e. $|\Psi_k^B(t)\rangle = |\Psi_k^F(t)\rangle = 0$ for $k \neq 1$ which is expanded in terms of the time-dependent basis of Eq. (3) consisting of different time-dependent variationally optimized SPFs.

C. Correlation measures

To investigate the role of intraspecies correlations, at the one-body level, during the interaction quench dynamics of the BF mixture we utilize the spatial first order coherence function [80, 103, 104]

$$g_\sigma^{(1)}(x, x'; t) = \frac{\rho_\sigma^{(1)}(x, x'; t)}{\sqrt{\rho_\sigma^{(1)}(x; t)\rho_\sigma^{(1)}(x'; t)}}. \tag{7}$$

In this expression, $\rho_\sigma^{(1)}(x, x'; t) = \langle \Psi(t) | \hat{\Psi}^{\sigma\dagger}(x) \hat{\Psi}^\sigma(x') | \Psi(t) \rangle$ is the σ species one-body reduced density matrix while $\rho_\sigma^{(1)}(x; t) \equiv \rho_\sigma^{(1)}(x, x' = x; t)$ denotes the corresponding one-body density. Also, $\hat{\Psi}^B(x)$ and $\hat{\Psi}^F(x)$ refer to the corresponding bosonic and fermionic field operators at position x satisfying the standard commutation and anti-commutation relations respectively [75]. Most importantly, the one-body coherence function $|g_\sigma^{(1)}(x, x'; t)|$ takes values in the

interval $[0, 1]$ and provides a degree of the deviation of the MB state from a product state for the set of coordinates x, x' . Indeed, two distinct spatial regions denoted e.g. by R and R' , where $R \cap R' = \emptyset$, exhibiting $|g_\sigma^{(1)}(x, x'; t)| = 1$, when $x \in R$ and $x' \in R'$, are termed fully coherent. In this case, the absence of one-body correlations in these regions can be inferred. However, when $|g_\sigma^{(1)}(x, x'; t)| < 1$ for $x \in R$ and $x' \in R'$ the regions are referred to as partially incoherent. Here, the aforementioned inequality signifies the emergence of one-body intraspecies correlations. Another interesting situation is when full coherence occurs within a spatial region R , i.e. when $|g^{(1),\sigma}(x, x'; t)|^2 \approx 1$ $x, x' \in R$, while perfect incoherence takes place between different spatial regions R, R' , when $|g^{(1),\sigma}(x, x'; t)|^2 \approx 0$ with $x \in R, x' \in R'$ and $R \cap R' = \emptyset$. This latter case suggests the emergence of Mott-like correlations [80, 88, 92] into the system and often indicates the spatial localization of the underlying structures building upon the respective one-body density [80, 81, 88].

To monitor the effective interactions between the non-interacting fermionic impurities in the course of the evolution we employ their relative distance [63]

$$D(t) = \frac{\int dx_1 dx_2 |x_1 - x_2| \rho_{FF}^{(2)}(x_1, x_2; t)}{\langle \Psi_{MB}(t) | \hat{N}_F (\hat{N}_F - 1) | \Psi_{MB}(t) \rangle}, \tag{8}$$

Here, $\rho_{FF}^{(2)}(x_1, x_2; t) = \langle \Psi_{MB}(t) | \Psi^{F\dagger}(x_1) \Psi^{F\dagger}(x_2) \Psi^F(x_1) \Psi^F(x_2) | \Psi_{MB}(t) \rangle$ is the diagonal two-body intraspecies reduced density matrix. This quantity provides the probability of finding the two fermions at the positions x_1 and x_2 at time t [80, 81]. Also, \hat{N}_F is the number operator that measures the number of fermions. Most importantly, $D(t)$ can be directly probed experimentally by performing *in-situ* spin-resolved single-shot measurements on the fermionic state [105]. In particular, each image provides an estimate of $D(t)$ between the fermionic impurities given that their position uncertainty is relatively small [105]. Then, $D(t)$ is obtained by averaging over several such images.

To quantify the degree of both intra- and interspecies correlations during the nonequilibrium dynamics we calculate the fragmentation of the σ -species and the entanglement between the species of the BF mixture [81, 106, 107]. This investigation allows us to infer about the proximity of the MB state [Eq. (2)] to a MF one [see Eq. (4)]. The presence of interspecies correlations or entanglement is designated by the values of the higher than the first Schmidt coefficients, i.e. $\lambda_k(t)$ with $k > 1$. Recall that $\lambda_k(t)$ are the eigenvalues of the species reduced density matrix $\rho^{N_\sigma}(\vec{x}^\sigma, \vec{x}'^\sigma; t) = \int d^{N_{\sigma'}} x^{\sigma'} \Psi_{MB}^*(\vec{x}^\sigma, \vec{x}'^\sigma; t) \Psi_{MB}(\vec{x}'^\sigma, \vec{x}^\sigma; t)$, with $\vec{x}^\sigma = (x_1^\sigma, \dots, x_{N_{\sigma-1}}^\sigma)$, and $\sigma \neq \sigma'$ [see also Eq. (2)]. Accordingly, the system is termed species entangled or interspecies correlated when more than a single eigenvalues of ρ^{N_σ} are macroscopically populated, otherwise it is non-entangled [see also the discussion around Eq.

2)]. A commonly used measure to identify the degree of species entanglement constitutes the Von-Neumann entropy [48, 81, 107]

$$S_{VN}(t) = - \sum_{k=1}^D \lambda_k(t) \ln[\lambda_k(t)]. \quad (9)$$

Note here that within the MF limit $S_{VN}(t) = 0$ holds since $\lambda_1(t) = 1$, while for a MB state where more than one λ_k contribute $S_{VN}(t) \neq 0$.

To unveil the fragmented or intraspecies correlated nature of each species we resort to the eigenvalues, $n_i^\sigma(t) = \int dx |\phi_i^\sigma(x; t)|^2$, of the σ -species one-body reduced density matrix, $\rho_\sigma^{(1)}(x, x'; t)$ [82, 104]. Note that $\phi_i^\sigma(x; t)$ are the so-called natural orbitals. It can be shown that when $\Psi_{MB}(\vec{x}^F, \vec{x}^B; t) \rightarrow \Psi_{MF}(\vec{x}^F, \vec{x}^B; t)$, see also Eq. (2) and Eq. (4), the fermionic and bosonic natural populations obey $\sum_{i=1}^{N_F} n_i^F(t) = 1$, $n_{i>N_F}^F(t) = 0$ and $n_1^B(t) = 1$, $n_{i>1}^B(t) = 0$ respectively. As a result, when more than N_F (one) fermionic (bosonic) natural orbitals are significantly populated the system is referred to as fragmented and the corresponding degree of fragmentation can be quantified as follows

$$F_F(t) = 1 - \sum_{i=1}^{N_F} n_i^F(t) \quad \text{and} \quad F_B(t) = 1 - n_1^B(t). \quad (10)$$

These constitute theoretical tools for the identification of the occupation of the $d_F - N_F$ and $d_B > 1$ least occupied fermionic and bosonic natural orbitals respectively, and thus of the deviation of the MB state from the MF one when $F_F(t) > 0$ and $F_B(t) > 0$.

III. QUENCH INDUCED DYNAMICS

In the following we investigate the interspecies interaction quench dynamics of the particle imbalanced BF mixture. The emergent nonequilibrium dynamics is explored both in the MF approximation [see Eq. (4)] and in the MB approach [see Eq. (2) and Eq. (3)]. Throughout this work we consider a BF mixture consisting of $N_B = 100$ bosons and $N_F = 2$ spin polarized fermionic impurities. In particular, the system is initialized in its weakly interacting ground state characterized by $g_{BB} = 0.5$ and $g_{BF} = 0.1$, unless it is stated otherwise. To induce the dynamics we perform an interspecies interaction quench from $g_{BF} = 0.1$ to a strongly interacting state such that $g_{BF} > g_{BB}$ and thus a phase separation process between the two components is favored (see also the discussion below).

A. Ground state of the BF mixture

Before delving into the nonequilibrium dynamics of the BF mixture it is instructive to briefly analyze its

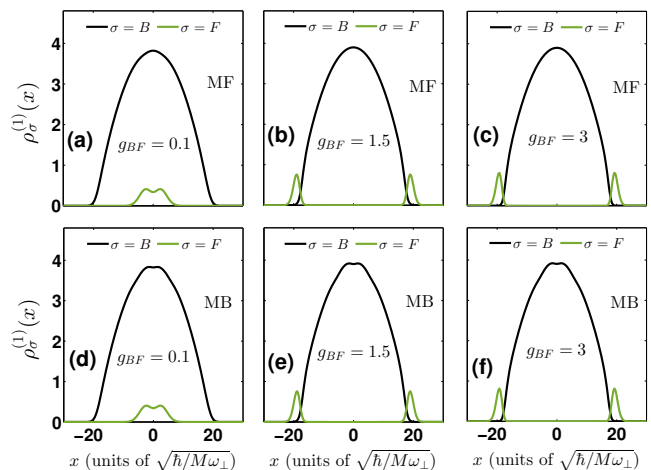


FIG. 1. One-body density $\rho_\sigma^{(1)}(x)$ of the ground state of the σ -species of the BF mixture for varying interspecies repulsions g_{BF} within (a), (b), (c) the MF approximation and (d), (e), (f) the MB approach. The BF mixture consists of $N_B = 100$ bosons and $N_F = 2$ fermions with $g_{BB} = 0.5$ and it is trapped in a harmonic oscillator potential with $\omega = 0.1$. Densities are expressed in units of $\sqrt{M\omega_\perp/\hbar}$.

ground state properties for fixed intraspecies interactions, $g_{BB} = 0.5$, and varying interspecies interactions g_{BF} . The mixture is confined in a harmonic oscillator potential of frequency $\omega = 0.1$ and it is prepared in its corresponding repulsively interacting ground state as described by the Hamiltonian of Eq. (1). To obtain the ground state of Eq. (1) we use either imaginary time propagation or improved relaxation [82, 100] within ML-MCTDH.

To explore the ground state properties of the BF mixture we employ the σ -species single-particle density $\rho_\sigma^{(1)}(x)$ [see also Eq. (7)]. Figure 1 presents $\rho_\sigma^{(1)}(x)$ within the MF approximation [Figs. 1 (a)-(c)] and on the MB level [see Figs. 1 (d)-(g)] for different interspecies interaction strengths and fixed $g_{BB} = 0.5$. In all cases $\rho_B^{(1)}(x)$ possesses the form of a Thomas-Fermi profile and it is almost insensitive to the value of g_{BF} . In particular, for an increasing interspecies repulsion the Thomas-Fermi profile becomes slightly more compressed and accordingly its maximum at $x = 0$ acquires a larger value [hardly discernible in Fig. 1]. Note also that due to the particle imbalance the bosons, being the majority species, exhibit a broader single-particle density distribution when compared to the fermions. Thus, $\rho_F^{(1)}(x)$ shows a much smaller amplitude than $\rho_B^{(1)}(x)$ and its shape depends crucially on g_{BF} [83–86]. More specifically, within the weakly interspecies interaction regime, $g_{BF} = 0.1$, $\rho_F^{(1)}(x)$ resides well inside the edges of $\rho_B^{(1)}(x)$ and therefore the two species are miscible since their spatial overlap is finite [Figs. 1(a), (d)]. For increasing interspecies repulsion, e.g. $g_{BF} = 1.5$, $\rho_F^{(1)}(x)$ splits into two den-

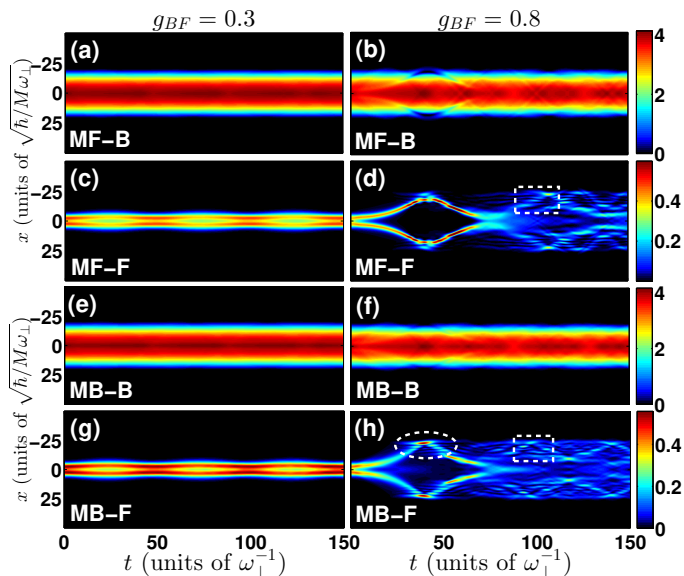


FIG. 2. Time-evolution of the $\sigma = B, F$ -species (see legends) one-body density, $\rho_\sigma^{(1)}(x; t)$, of the BF mixture following an interspecies interaction quench within (a)-(d) the MF approximation and (e)-(h) the MB approach. The postquench interspecies interaction strengths correspond to (a), (c), (e), (g) $g_{BF} = 0.3$ and (b), (d), (f), (h) $g_{BF} = 0.8$. Dashed rectangles in (d), (h) mark the presence of several local minima in $\rho_F^{(1)}(x; t)$, while the dashed ellipse in (h) indicates the splitting of $\rho_F^{(1)}(x; t)$ for $x < 0$. The system consists of $N_B = 100$ bosons and $N_F = 2$ fermions trapped in a harmonic oscillator potential and it is initialized in its ground state for $g_{BF} = 0.5$ and $g_{BF} = 0.1$.

sity branches each one located either at the right or the left edge of $\rho_B^{(1)}(x)$ respectively [Figs. 1(b), (e)]. This behavior indicates the immiscible character of the mixture for strong g_{BF} , i.e. the spatial overlap between $\rho_B^{(1)}(x)$ and $\rho_F^{(1)}(x)$ is almost zero, a character that remains as such for even stronger g_{BF} [see Figs. 1(c), (f)]. Also, by carefully inspecting $\rho_F^{(1)}(x)$ for these strong interactions we can deduce that for an increasing g_{BF} the density peaks of $\rho_F^{(1)}(x)$ become slightly more localized and their relative distance slightly decreases [hardly discernible in Figs. 1(b) and (c)]. Another important observation here is that both $\rho_B^{(1)}(x)$ and $\rho_F^{(1)}(x)$ are essentially the same within the MF approximation and the MB approach. Indeed the inclusion of correlations causes only small deviations in the corresponding ground state density profiles. For instance, a shallow local minimum appears in $\rho_B^{(1)}(x)$ around $x = 0$ within the MB approach which is absent at the MF level, e.g. compare Figs. 1(b) and (e). The existence of such a local minimum in $\rho_B^{(1)}(x)$ suggests a minor involvement of higher-excited states of the harmonic oscillator for the correct characterization of the ground state.

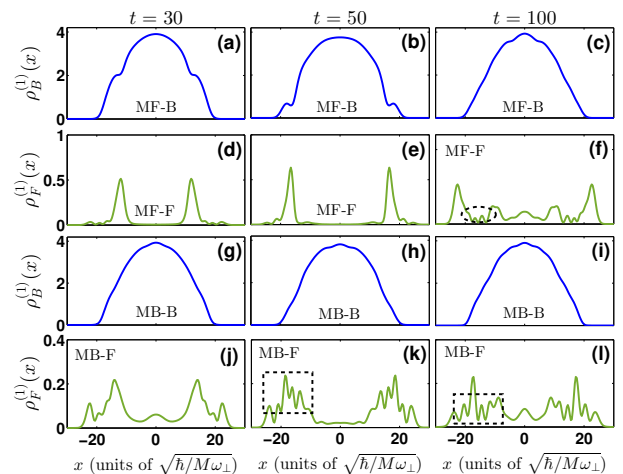


FIG. 3. One-body density profiles, $\rho_\sigma^{(1)}(x; t)$, of the $\sigma = B, F$ species of the BF mixture at different time instants following an interspecies interaction quench from $g_{BF} = 0.1$ to $g_{BF} = 0.8$ (see legends). (a)-(c) [(d)-(f)] present $\rho_B^{(1)}(x; t)$ [$\rho_F^{(1)}(x; t)$] within the MF approximation. (g)-(i) [(j)-(l)] show $\rho_B^{(1)}(x; t)$ [$\rho_F^{(1)}(x; t)$] determined in the MB approach. The dashed ellipse in (f) and the dashed rectangles in (k), (l) indicate the presence of local minima in $\rho_F^{(1)}(x; t)$ for $x < 0$ determined at the MF and the MB level respectively. The remaining system parameters are the same as in Fig. 2. The densities are given in units of $\sqrt{M\omega_\perp}/\hbar$.

B. Single-particle density evolution

Having analyzed the ground state properties of the BF mixture for increasing interspecies interactions, we next investigate its nonequilibrium dynamics following a sudden change of g_{BF} from $g_{BF} = 0.1$ towards stronger repulsive interspecies interactions. Figures 2 and 4 show $\rho_\sigma^{(1)}(x; t)$ of the bosonic and fermionic species both within the MF and the MB level for different characteristic postquench interspecies interaction strengths. As it can be seen, the dynamics of the mixture on the single-particle level can be categorized into four distinct interaction regions. Most importantly, the structures building upon $\rho_\sigma^{(1)}(x; t)$ differ considerably between the MF and the MB approach, especially when $g_{BF} > g_{BF}$. In particular, for a quench within the weak interspecies interaction regime such that $g_{BF} < g_{BF}$, e.g. $g_{BF} = 0.3$, both $\rho_B^{(1)}(x; t)$ and $\rho_F^{(1)}(x; t)$ exhibit a breathing motion [see Figs. 2(a), (c)] characterized by a frequency $\omega_{br}^B \approx 0.21 \equiv 2\omega$ and $\omega_{br}^F \approx 0.16$ respectively [86, 87]. Note that the total external potential of the fermionic impurities is, to a very good approximation, the effective potential created by the harmonic oscillator and the density of bosons [77, 108], i.e. $V_{eff} = \frac{1}{2}m\omega^2 x^2 + g_{BF}\rho_B^{(1)}(x)$, with $\rho_B^{(1)}(x)$ being the bosonic single-particle density at $t = 0$. Hence, assuming the Thomas-Fermi approximation for $\rho_B^{(1)}$ we obtain the following effective trap-

ping frequency of the impurities $\omega_{eff} = \omega\sqrt{1 - \frac{g_{BF}}{g_{BB}}}$ and therefore their corresponding effective breathing frequency would be $\omega_{br}^{eff,F} = 2\omega_{eff} = 0.16$ which is indeed in a very good agreement with the numerically obtained ω_{br}^F . We remark that this effective potential approximation is adequate only for small interspecies interactions where the entanglement between the species is weak [see Sec. III F] and the impurities do not probe the edges of the bosonic cloud, see also [66, 77] for more details. Moreover, $\rho_F^{(1)}(x;t)$ resides within $\rho_B^{(1)}(x;t)$ throughout the evolution indicating the miscible character of the dynamics. This behavior of $\rho_\sigma^{(1)}(x;t)$ occurs both at the MF [Figs. 2(a), (c)] and at the MB level [Figs. 2(e), (g)] since the degree of intra- and interspecies correlations is negligible here [see also Sec. III F].

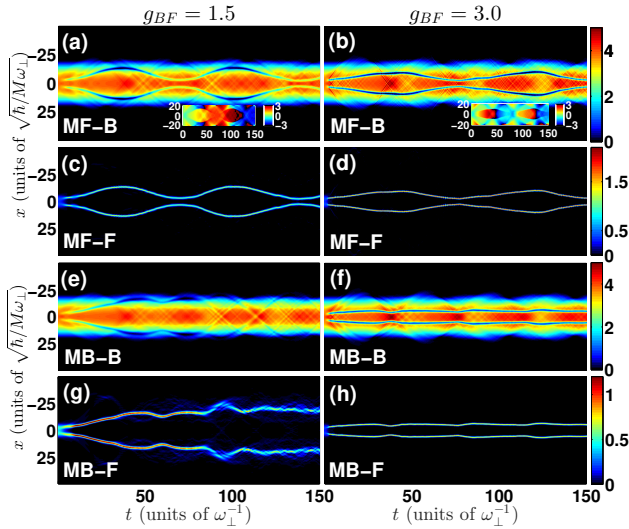


FIG. 4. Spatiotemporal evolution of the $\sigma = B, F$ -species one-body density, $\rho_\sigma^{(1)}(x;t)$, of the BF mixture upon considering an interspecies interaction quench within (a)-(d) the MF approximation and (e)-(h) the MB approach (see legends). The postquench interspecies interaction strength corresponds to (a), (c), (e), (g) $g_{BF} = 1.5$ and (b), (d), (f), (h) $g_{BF} = 3$. The insets in (a), (b) show the corresponding phases during the dynamics. The system consists of $N_B = 100$ bosons and $N_F = 2$ fermions trapped in a harmonic oscillator potential and it is initialized in its ground state characterized by $g_{BB} = 0.5$ and $g_{BF} = 0.1$.

Increasing the postquench interaction strength g_{BF} to a value larger than g_{BB} the impurities undergo a much more involved dynamics compared to the weakly interacting case, while the majority species performs a breathing motion [Figs. 2(b), (f)] again with $\omega_{br}^B \approx 0.21$. Focusing on the MF approximation we observe that directly after the quench $\rho_F^{(1)}(x;t)$ splits into two density branches [Figs. 3(d), (e)] that acquire finite momenta and travel towards the edges of the bosonic cloud [Figs. 2(b), (d) and Figs. 3(a), (b)]. Note that the appearance of these density branches is caused by the interaction quench which imports energy into the system. Reaching the edges of

$\rho_B^{(1)}(x;t)$ these density humps of $\rho_F^{(1)}(x;t)$ are reflected back towards the trap center. Subsequently, around $t \approx 70$, they collide at $x = 0$ and then show a dispersive behavior. In particular, directly after the collision $\rho_F^{(1)}(x;t)$ splits into several localized density humps, reflecting in this way its spatial delocalization, that are seen to propagate predominantly within $\rho_B^{(1)}(x;t)$ during evolution, see Fig. 2(d). This dispersive character of $\rho_F^{(1)}(x;t)$ is clearly captured and shown in the corresponding profile snapshots, see for instance the dashed ellipse in Fig. 3(f) and the relevant dashed rectangle in Fig. 2(d). In turn these localized humps indicate that $\rho_F^{(1)}(x;t)$ is in a superposition of several lower-lying excited states of the external potential into which the impurities are trapped. It is also important to note here that since the impurities probe the edges of the Thomas-Fermi radius of $\rho_B^{(1)}(x;t)$, the effective potential picture previously introduced is not sufficient to describe the observed dynamics. The same overall phenomenology is also observed at the MB level. However, important differences between the two approaches can be noticed especially in the time-evolution of $\rho_F^{(1)}(x;t)$. The most important feature here is that each of the two initially formed density branches [Fig. 3(j)] split into several density peaks [Figs. 3(k), (l)] of significantly lower intensity. This further splitting, that is in contrast to the MF outcome, occurs when each of the fermionic density humps approaches the edges of the BEC medium and persists even upon their return towards the trap center [see here the dashed ellipse in Fig. 2(h) and also the dashed rectangle in Fig. 3(k)]. This behavior, that is absent within the MF approximation, is attributed to correlations present in the interaction of the impurities with the bosonic bath. Moreover, the dispersive character of $\rho_F^{(1)}(x;t)$ is more pronounced at the MB level with the number of localized density humps being larger as compared to the MF description of the dynamics [compare e.g. Figs. 3(f) and (l)]. The latter observation indicates that the impurities are in a superposition of energetically higher excited states as compared to the MF scenario. Note also that $\rho_F^{(1)}(x;t)$ shown e.g. in Fig. 2(h) results from the correlated MB approach and a corresponding interpretation in terms of V_{eff} in this case provides only a crude picture of the impurity dynamics since V_{eff} does not contain any information about correlations.

Turning to even stronger postquench interaction strengths, e.g. $g_{BF} = 1.5$, the dynamical behavior of both the fermionic and the bosonic species changes drastically compared to the above discussed cases. Most importantly, the dynamics is severely different between the MF the MB approach as can be deduced by comparing Figs. 4(a), (c) to Figs. 4(e), (g) respectively. Inspecting $\rho_B^{(1)}(x;t)$ [Fig. 4(a)] and $\rho_F^{(1)}(x;t)$ [Fig. 4(c)] within the MF approximation we observe the spontaneous generation of two localized density peaks in $\rho_F^{(1)}(x;t)$ robustly propagating within the BEC medium repelling

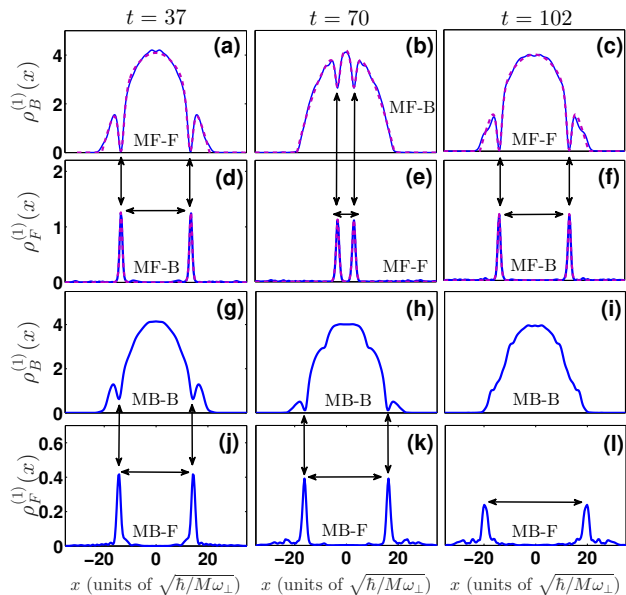


FIG. 5. Snapshots of the $\sigma = B, F$ species (see legend) one-body density, $\rho_\sigma^{(1)}(x; t)$, of the BF mixture at selected time instants (see legends) after an interspecies interaction quench from $g_{BF} = 0.1$ to $g_{BF} = 1.5$. (a)-(c) [(d)-(f)] show $\rho_B^{(1)}(x; t)$ [$\rho_F^{(1)}(x; t)$] within the MF approximation. (g)-(i) [(j)-(l)] illustrate $\rho_B^{(1)}(x; t)$ [$\rho_F^{(1)}(x; t)$] within the MB approach. The vertical double arrows indicate the corresponding DB pairs while the horizontal arrows show the relative distance between the fermions. The remaining system parameters are the same as in Fig. 4. The densities are expressed in units of $\sqrt{M\omega_\perp}/\hbar$.

and attracting one another, thus performing an oscillatory motion. These density humps are accompanied by the simultaneous formation of two density dips in $\rho_B^{(1)}(x; t)$ located at the same spatial regions and filled by the density peaks of the fermionic species. Such a filling mechanism resembles the formation of DB solitons in defocusing media which in our case oscillate within the parabolic trap with a period $T_{DB} \approx 69$ [see Fig. 4(c)]. Let us note in passing that for the specific chosen parameters of our system the spontaneous generation of DB solitons occurs at postquench interspecies interaction strengths larger than $g_{BF} = 0.9$. To provide evidence that indeed the structures building upon $\rho_B^{(1)}(x; t)$ possess a dark soliton character the spatio-temporal evolution of the relevant phase is illustrated in the inset of Fig. 4(a). Evidently, the entities formed exhibit a phase jump being multiple of π . To further support our above-mentioned arguments regarding the DB character of the quench generated structures we present in Figs. 5(a)-(c) and (d)-(f) profile snapshots of the single-particle densities $\rho_B^{(1)}(x; t)$ and $\rho_F^{(1)}(x; t)$ respectively at $t = 37$, $t = 70$ and $t = 102$ for a quench to $g_{BF} = 1.5$. To identify the occurrence of DB states we employ the exact in the so-called integrable limit single DB soliton

solution [109–112]. In this case the corresponding wavefunction ansatz for a dark and a bright soliton state reads $\Psi_B^l(x, t) = \cos \phi \tanh[D(x - x_0(t))] + i \sin \phi$ and $\Psi_F^l(x, t) = B \operatorname{sech}[D(x - x_0(t))] e^{ikx + i\theta(t)}$. Here, $\cos \phi$ and B denote the amplitude of the dark and the bright soliton respectively and D is their common inverse width. Moreover, $\sin \phi$ is the dark soliton's velocity, $x_0(t)$ is the soliton's center, $k = D \tan \phi$ is the constant wavenumber of the bright soliton, $\theta(t)$ its phase and l indexes the number of the DB pair. Since in our case two DB soliton pairs are spontaneously generated, we further assume that the wavefunction ansatz that describes such a two DB state is approximately given by $\Psi_B(x; t) = \Psi_B^1(x, t)\Psi_B^2(x, t)$ for the dark solitons developed in the bosonic component and $\Psi_F(x, t) = \Psi_F^1(x, t) + \Psi_F^2(x, t)$ for the bright states formed in the fermionic one. We use these expressions, and in particular $|\Psi_B(x, t)|^2$ and $|\Psi_F(x, t)|^2$, for the fits in the density profiles shown with dashed lines in Figs. 5(a)-(f). Evidently, a remarkably good agreement between the MF numerical simulations and the fitted profiles occurs [see also Table I], thus verifying that indeed the quench-induced structures possess a DB solitary wave character.

Having identified the formation of DB states at the MF level next let us inspect how the nonequilibrium dynamics is altered in the presence of correlations. As it can be seen both $\rho_B^{(1)}(x; t)$ [Figs. 4(e)] and $\rho_F^{(1)}(x; t)$ [Figs. 4(g)] are significantly different compared to their MF counterparts. In particular, after the quench $\rho_F^{(1)}(x; t)$ breaks into two distinct localized density peaks which travel towards the edges of $\rho_B^{(1)}(x; t)$. Within this time interval, $0 < t < 40$, the density peaks of $\rho_F^{(1)}(x; t)$ are accompanied by density dips in $\rho_B^{(1)}(x; t)$ resembling this way DB states. This situation is more evident in the corresponding profile snapshots of the densities [Figs. 5(g), (h), (j), (k)] where the density dips building upon the bosonic bath are filled by the density peaks formed in the fermionic species. However, when these localized pairs reach the edges of $\rho_B^{(1)}(x; t)$, instead of returning towards the trap center, they remain at the edges of the cloud while oscillating locally. As can be deduced by focusing our attention to the fermionic species [Fig. 4(g)] the observed oscillations are rather irregular and result in localized states whose amplitude is almost half the initial one [see also Fig. 5(l)]. Notice also that the initially formed density dips in $\rho_B^{(1)}(x; t)$ are hardly visible for evolution times $t > 100$, a result that is clearly seen in the profile snapshot presented in Fig. 5(i). The above observations suggest that the DB character of the states formed is significantly altered by the presence of correlations. This alteration is captured by the decaying amplitude of the dark states formed in the BEC.

Quenching the interspecies interactions to very strong values, e.g. $g_{BF} = 3$, we observe a significant alteration of the evolution of the BF mixture single-particle densities, compared to the $g_{AB} = 1.5$ case, especially at the MB level [Figs. 4 (f), (h)]. Evidently, within the MF

Two DB soliton pair characteristics			
		$t = 37$	$t = 102$
Dark	$\cos \phi$	1.341	1.320
	D	0.669	0.749
	$\sin \phi$	0.160	0.122
	x_0	13.390	13.580
	R_{TF}	20.790	21.060
Bright	B	0.878	0.909
	D	0.669	0.749
	x_0	13.450	13.570

TABLE I. Two DB soliton pair characteristics referring to different time instants of the dynamics of both species shown in Figs. 4 (c) and Figs. 5 (a), (d), (e) and (f). The parameters $\cos \phi$ and B refer to the amplitude of the dark and bright solitons respectively generated in the $\sigma = B$ and $\sigma = F$ species. Additionally, R_{TF} denotes the Thomas-Fermi radius of the BEC background. Note also that in all cases the accuracy of the fitting is 0.95.

approximation the formation of DB states can again be inferred. Notice, for instance, that the dark states are characterized by a phase jump being a multiple of π [see the inset of Fig. 4 (b)]. However, for these strong interactions the period ($T_{DB} \approx 74$) and the amplitude of the DB oscillation become larger and smaller respectively as compared to the $g_{BF} = 1.5$ quench scenario, see Figs. 4 (c) and (d). Indeed, for an increasing postquench g_{BF} the degree of the dynamical phase separation between the two species is enhanced, see also the discussion in Sec. III C and Fig. 6 (a). The latter dynamical process is manifested by the spontaneous generation of dark soliton structures in the bosonic gas and bright solitons of the fermionic component. Moreover, as a result of the larger degree of the dynamical phase separation for increasing g_{BF} the spontaneously formed dark solitons are found to be deeper [e.g. see $\rho_B^{(1)}(x; t = 2)$ in Figs. 4 (a) and (b)] and thus slower, with the respective bright ones being in turn more spatially localized, see for instance $\rho_F^{(1)}(x; t = 2)$ in Figs. 4 (c) and (d). The fact that these dark structures appear to be deeper and the bright solitons more spatially localized suggests that their inverse width D becomes larger. Indeed, measuring the inverse width D of the solitons and the velocity ($\sin \phi$) of the dark component via fitting to their analytical waveforms it is found that for $g_{BF} = 3$ only a slight increase of D occurs while $\sin \phi$ decreases significantly as compared to the $g_{BF} = 1.5$ case. Recall that [109] the velocity of a DB pair is given by $\dot{x}_0(t) = D \tan \phi$. However for $g_{BF} = 3$ the amplitude of the dark soliton, namely $\cos \phi$, increases significantly as compared to the $g_{BF} = 1.5$ scenario, see also Figs. 4 (a), (b). As a consequence $\dot{x}_0(t)$ reduces and therefore the observed oscillations of the DB pair are of smaller amplitude. Also, for a DB soliton it is known [109, 112] that its oscillation period is inversely proportional to the chemical potential of the dark component or equivalently the Thomas-Fermi radius of the BEC background that hosts the dark states. Inspecting

again the ground state of $\rho_B^{(1)}(x)$ for larger g_{BF} we can deduce that the corresponding Thomas-Fermi radius becomes smaller for a larger g_{BF} [compare Figs. 1 (a)-(c)], a behavior that explains the observed increased oscillation period of the DB soliton. In contrast, at the MB level we observe that after the quench $\rho_F^{(1)}(x; t)$ splits into two branches which repel each other at the very early stages of the dynamics ($0 < t < 5$) and then for later evolution times oscillate with a very small amplitude around a mean value and tend to an almost steady state (see also the discussion in Secs. III D, III E and III H). On the other hand, the majority species forms density dips at the spatial regions where the density peaks of the impurities are located. Therefore, the quench generated entities resemble a two DB solitary wave state which in contrast to its MF counterpart tends to approach a stationary state [109, 110].

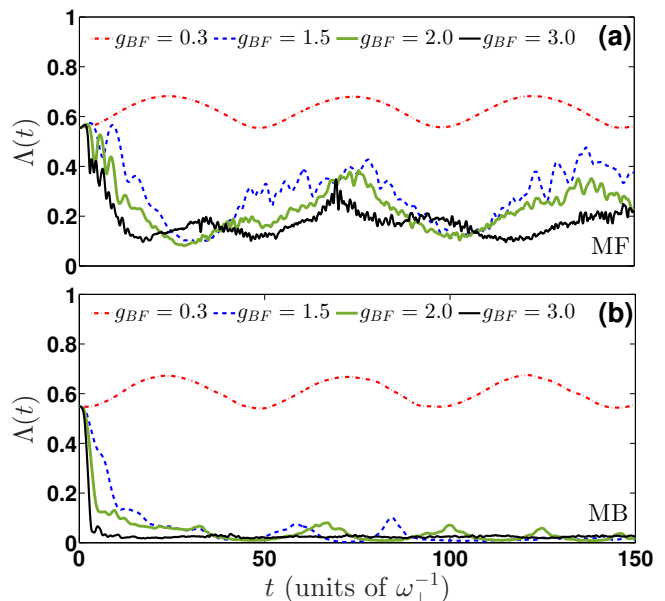


FIG. 6. Dynamics of the overlap function, $\Lambda(t)$, between the bosonic and the fermionic clouds for $g_{BB} = 0.5$ and varying $g_{BF} = 0.3, 1.5, 2, 3$ (see legend) within (a) the MF and (b) the MB approach. The remaining system parameters are the same as in Fig. 2.

C. Degree of miscibility

To appreciate the degree of miscibility or immiscibility between the species of the BF mixture, at the one-body level we resort to the overlap integral function $\Lambda(t)$ [80, 113] which is defined as

$$\Lambda(t) = \frac{\left[\int dx \rho_B^{(1)}(x; t) \rho_F^{(1)}(x; t) \right]^2}{\left[\int dx (\rho_B^{(1)}(x; t))^2 \right] \left[\int dx (\rho_F^{(1)}(x; t))^2 \right]}. \quad (11)$$

In particular, $\Lambda = 0$ and $\Lambda = 1$ designate zero and complete spatial overlap of the two species respectively. Figures 6 (a), (b) illustrate $\Lambda(t)$ for different postquench interspecies interaction strengths at the MF and the MB level respectively. For weak values of g_{BF} , such that $g_{BF} < g_{BB}$, the overlap integral oscillates in time (reflecting this way the breathing motion e.g. of the bosonic cloud) around the value 0.6 demonstrating a tendency towards miscibility both at the MF and the MB level. This behavior of $\Lambda(t)$ changes for quenches that satisfy $g_{BF} > g_{BB}$. Regarding the evolution within the MF approximation, independently of $g_{BF} > g_{BB}$, $\Lambda(t)$ shows a decreasing behavior at the very early stages of the dynamics and subsequently performs oscillations [resembling this way the overall motion of the DB state, see Figs. 4 (a), (c)] around a mean value which is smaller for a larger postquench g_{BF} , e.g. it is 0.22 for $g_{BF} = 1.5$ and 0.18 for $g_{BF} = 3$. Accordingly, also the amplitude of the oscillations of $\Lambda(t)$ becomes smaller for increasing g_{BF} indicating an overall tendency for a larger degree of phase separation for stronger postquench interactions. It is also worth noticing at this point that $\Lambda(t) \neq 0$ even for $g_{BF} = 3$, thus evincing that complete phase separation can not be achieved at the MF level. However, at the MB level $\Lambda(t)$ shows a completely different behavior and its magnitude is always smaller than its MF counterpart, in particular compare Figs. 6 (a) and (b) for a fixed $g_{BF} > g_{BB}$. Indeed, entering the strong interspecies interaction regime, $g_{BF} > 1.5$, we observe that $\Lambda(t)$ exhibits a fast decrease and then for later evolution times approaches zero thus testifying a complete phase separation between the two species.

D. Relative distance between the impurities

To estimate the nature of the interactions induced by the presence of the bosons between the two non-interacting fermionic impurities we determine their relative distance, $D(t)$, during the dynamics [see also Eq. (8)]. Recall, that this quantity can be probed experimentally via in-situ spin-resolved single-shot measurements performed on the state of the impurities [105]. The time-evolution of $D(t)$ is shown in Figs. 7 (a), (b) for different g_{BF} within the MF and the MB approach respectively. For very weak interactions, e.g. $g_{BF} = 0.3$, and in both approaches $D(t)$ takes small values since the impurities are very close in this case and undergoes small amplitude oscillations in time reflecting this way the breathing motion of the impurities. Focusing on the MF approximation we observe that for every $g_{BF} \gg g_{BB}$ the relative distance exhibits an increasing tendency at the initial stages of the dynamics while for later times oscillates with a decreasing amplitude for larger g_{BF} . The initially increasing tendency of $D(t)$ essentially demonstrates the repulsive tendency of the impurity density branches already evident in $\rho_F^{(1)}(x;t)$ [e.g. see Fig. 4 (c)], which is a consequence of the effective potential created by $\rho_B^{(1)}$. The

subsequent fluctuating behavior of $D(t)$ reflects the oscillatory motion of the previously discussed bright states. However at the MB level the behavior of $D(t)$ changes drastically. In particular for a quench to $g_{BF} \gg g_{BB}$, $D(t)$ initially increases reflecting the presence of repulsive induced interactions captured by $\rho_F^{(1)}(x;t)$ [see also Fig. 4 (g)] while small amplitude oscillations occur during evolution, with an overall increasing tendency. For very strong postquench interaction strengths, e.g. for $g_{BF} = 3$, the amplitude of these oscillations diminishes and $D(t)$ acquires an almost constant value [see also Fig. 4 (h)] suggesting that the impurities tend to approach a stationary state.

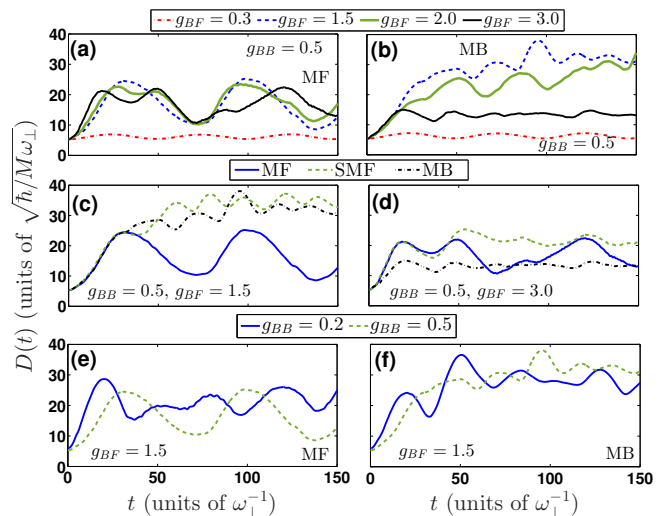


FIG. 7. Time-evolution of the relative distance, $D(t)$, between the two fermionic impurities following an interspecies interaction quench of the BF mixture. (a), (b) shows $D(t)$ for fixed $g_{BB} = 0.5$ and varying $g_{BF} = 0.3, 1.5, 2, 3$ calculated within (a) the MF and (b) the MB approach. (c), (d) illustrates $D(t)$ for $g_{BB} = 0.5$ and for (c) $g_{BF} = 1.5$ and (d) $g_{BF} = 3.0$ within different levels of approximation (see legend). (e), (f) presents $D(t)$ for $g_{BF} = 1.5$ and varying $g_{BB} = 0.2, 0.5$ (see legend) at (e) the MF and (f) the MB level. Note that the Thomas-Fermi radius of the bosonic gas corresponds to $R_{TF} = 14.4$ at $g_{BB} = 0.2$ and $R_{TF} = 19.6$ at $g_{BB} = 0.5$. The other system parameters are the same as in Fig. 2.

To expose the significance of the inclusion of different levels of correlations in the dynamical behavior of the relative distance we next measure $D(t)$ between the fermionic impurities by systematically taking into account different orders of correlations. In particular, we determine $D(t)$ within the MF approximation where all correlations are neglected [see Eq. (4)], the SMF approximation where only intraspecies correlations are included [see Eq. (6)] and in the MB approach where all correlations are incorporated [see Eq. (2)]. Figures 7 (c), (d) present $D(t)$ within the above-mentioned approaches for $g_{BF} = 1.5$ and $g_{BF} = 3$ respectively. As it can be seen, for $g_{BF} = 1.5$ all approaches capture the initial ($0 < t < 35$) increase of $D(t)$ but for later times signifi-

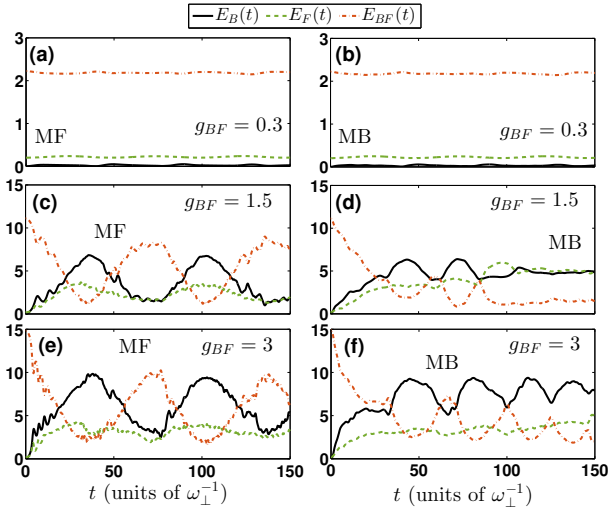


FIG. 8. Expectation value of the energy of the bosons $E_B(t)$, the fermions $E_F(t)$ and their mutual interaction $E_{BF}(t)$ (see legend) following an interspecies interaction quench from $g_{BF} = 0.1$ to (a), (b) $g_{BF} = 0.3$, (c), (d) $g_{BF} = 1.5$ and (e), (f) $g_{BF} = 3$. The calculations are performed within (a), (c), (e) the MF approximation and (b), (d), (f) the MB approach. The other system parameters are the same as in Fig. 2.

cant deviations occur. Indeed, at the MF level $D(t)$ undergoes large amplitude oscillations in time, while at the SMF and MB level $D(t)$ shows an overall increasing tendency performing also small amplitude oscillations. Importantly here the SMF approximately captures the overall behavior of $D(t)$ but overestimates its values. Turning to stronger interactions, $g_{BF} = 3$ we observe that both the MF and the SMF fail to capture the MB dynamics of $D(t)$ [Fig. 7 (d)]. Concluding we can clearly infer that both intra- and interspecies correlations are important for the adequate description of $D(t)$. The latter in turn dictates a much stronger repulsion between the impurities for intermediate g_{BF} values when compared to a MF description of the out-of-equilibrium dynamics.

The behavior of $D(t)$ for different intraspecies interaction strengths, g_{BB} , of the bosonic medium but for fixed $g_{BF} = 1.5$ is illustrated in Figs. 7 (e), (f) within the MF and the MB approach respectively. In both cases and for all g_{BB} values that we have addressed it is found that at initial times $D(t)$ increases and consecutively oscillates as time evolves. However, this initial increase occurs faster for weaker intraspecies interactions. In particular, $D(t)$ reaches a local maximum with $D(t \approx 20) \approx 29$ and $D(t \approx 20) \approx 23$ within the MF and the MB approach respectively for $g_{BB} = 0.2$. In contrast to the above and e.g. for $g_{BB} = 0.5$, the first maximum appears for comparatively larger times. Here, $D(t \approx 31) \approx 25$ and $D(t \approx 50) \approx 29$ for the MF and the MB case respectively. It is worth mentioning that a larger g_{BB} implies also a larger Thomas-Fermi radius, and hence size, of the BEC. For instance, the Thomas-Fermi radius at $g_{BB} = 0.2$ is

$R_{TF} \approx 14$ while at $g_{BB} = 0.5$ becomes $R_{TF} \approx 19$. Therefore, the observed differences in the initial increase and subsequent oscillations of $D(t)$ for varying g_{BB} can be attributed to the fact that a larger g_{BB} , while fixing the particle number N_B , gives rise to a more dilute repulsive environment. The latter in turn exerts a weaker repulsive effective force on the impurities compared to the case of a smaller g_{BB} . Thus, a stronger g_{BB} slows down the initial expansion of the impurities and vice versa. The latter effect takes place at both the MF and the MB level. Moreover, for evolution times $t > 80$ almost damped oscillations of $D(t)$ for all g_{BB} values occur when correlations are present. A behavior that is absent within the MF treatment (see also the discussion below).

E. Interspecies energy transfer

To further analyze and understand the nonequilibrium dynamics of the BF mixture occurring for different postquench interspecies interaction strengths below we focus on the study of the distinct energy contributions [65, 77]. More specifically, the normalized energy of the bosonic species is $E_B(t) = \langle \Psi(t) | \hat{T}_B + \hat{V}(x) + \hat{H}_{BB} | \Psi(t) \rangle - \langle \Psi(0) | \hat{T}_B + \hat{V}(x) + \hat{H}_{BB} | \Psi(0) \rangle$, and for the fermionic impurities corresponds to $E_F(t) = \langle \Psi(t) | \hat{T}_F + \hat{V}(x) | \Psi(t) \rangle$. Additionally, the interspecies interaction energy is $E_{BF}(t) = \langle \Psi(t) | \hat{H}_{BF} | \Psi(t) \rangle$. Note that the kinetic and the potential energy operators of the $\sigma = B, F$ species are $\hat{T}_\sigma = -\int dx \hat{\Psi}^{\sigma\dagger}(x) \frac{\hbar^2}{2M} \left(\frac{d}{dx}\right)^2 \hat{\Psi}^\sigma(x)$ and $\hat{V}_\sigma = \int dx \hat{\Psi}^{\sigma\dagger}(x) \frac{1}{2} M \omega^2 x^2 \hat{\Psi}^\sigma(x)$ respectively. The operators of the intra- and interspecies interactions read $\hat{H}_{BB} = g_{BB} \int dx \hat{\Psi}^{B\dagger}(x) \hat{\Psi}^{B\dagger}(x) \hat{\Psi}^B(x) \hat{\Psi}^B(x)$ and $\hat{H}_{BF} = g_{BF} \int dx \hat{\Psi}^{B\dagger}(x) \hat{\Psi}^{F\dagger}(x) \hat{\Psi}^F(x) \hat{\Psi}^B(x)$. Also, $\hat{\Psi}^\sigma(x) [\hat{\Psi}^{\sigma\dagger}(x)]$ denotes the σ species field operator that annihilates [creates] a σ species particle at position x .

The time-evolution of the above-mentioned energy contributions is shown in Fig. 8 for a varying g_{BF} both within the MF approximation [Figs. 8 (a), (c), (e)] and in the MB approach [Figs. 8 (b), (d), (f)]. Referring to weak postquench interactions, e.g. $g_{BF} = 0.3$, all energy parts are mainly constant throughout the dynamics and $E_B(t) < E_F(t) < E_{BF}(t)$ holds. This result being almost identical in both the MF and the MB scenario [Figs. 8 (a), (b)] suggests that in the weak interaction regime the role of correlations is negligible. Turning to stronger interactions, e.g. $g_{BF} = 1.5$, we observe that the different energy contributions undergo a much more involved dynamics in both approaches [Figs. 8 (c), (d)]. Indeed, when all particle correlations are neglected $E_{BF}(t)$ decreases while $E_B(t)$ and $E_F(t)$ increase at the initial stages of the dynamics ($0 < t < 35$). For later times all the different energy contributions exhibit large amplitude oscillations in time being more pronounced for $E_B(t)$. In particular, $E_B(t)$ and $E_F(t)$ oscillate in-phase with respect to one another and both are out-of-phase

with $E_{BF}(t)$. This latter behavior suggests that a periodic energy transfer process from the fermionic impurities (bright solitons) to the bosonic environment occurs as a consequence of the DB oscillatory motion. More specifically, when the bright solitons travel towards the edges of the BEC medium [see also Fig. 4 (c)] they acquire more kinetic energy, and thus $E_F(t)$ increases, and convey energy to the bosonic bath resulting to an increase of the energy, $E_B(t)$, of the latter. This energy stems from the large E_{BF} at $t = 0$ which subsequently decreases. On the other hand, when the bright solitons are reflected back to the trap center [Fig. 4 (c)] they become slower [109, 110] and therefore $E_F(t)$ and consequently $E_B(t)$ become smaller while $E_{BF}(t)$ increases since the interaction between the two species is larger. However, the dynamical behavior of the corresponding energy contributions within the correlated treatment is drastically different when compared to its MF counterpart [Figs. 8 (c) and (d)]. Recall that such a deviation is already evident from the corresponding single-particle density evolution, see e.g. Figs. 4 (c) and (g). Initially, $0 < t < 35$, $E_{BF}(t)$ reduces while $E_F(t)$ and E_B increase. Indeed, within this time interval the two fermionic density branches move to the edges of the bosonic bath [Fig. 4 (g)] with a large kinetic energy and as a result devolve energy to the latter. For $35 < t < 95$, $E_B(t)$ and $E_{BF}(t)$ oscillate out-of-phase whilst $E_F(t)$ increases while performing small amplitude oscillations. Therefore the fermionic impurities transfer a part of their energy to the bosonic gas. It is in this time interval that $\rho_F^{(1)}(x;t)$ resides close to the boundaries of $\rho_B^{(1)}(x;t)$ and still weakly interacts with the BEC. Deeper in the evolution, $t > 95$, all energy components acquire an almost constant value with $E_B(t) \equiv E_F(t) < E_{BF}(t)$. Recall that for $t > 95$ $\rho_F^{(1)}(x;t)$ resides at the edges of $\rho_B^{(1)}(x;t)$ and therefore the two species barely interact.

Inspecting the energies for even stronger interactions, $g_{BF} = 3$, [Figs. 8 (e), (f)] we can deduce that an overall similar to the above-described dynamics takes place. Focusing on the MF approximation we observe that at the initial time period ($0 < t < 30$) the decrease of $E_{BF}(t)$ is accompanied by a simultaneous increase of both $E_F(t)$ and $E_B(t)$ with the magnitude of the latter found to be larger. We remark that in this time interval the bright solitons move to the edges of the BEC cloud thus becoming faster [Fig. 4 (d)] and transferring energy to the bosonic bath. For $t > 30$, $E_F(t)$ and $E_B(t)$ oscillate in-phase with each other but out-of-phase with $E_{BF}(t)$. Note also the much larger oscillation amplitude of $E_B(t)$ as compared to $E_F(t)$. Overall when the bright solitons travel to the edges (core) of the BEC medium they acquire more (less) kinetic energy. The corresponding $E_{BF}(t)$ becomes smaller (larger), and the bosonic bath gains (loses) energy [see also Figs. 4 (b), (d)]. On the contrary, turning to the MB description the energies show again a quite different behavior to the one observed in the MF approximation. For times up to $t = 10$, $E_{BF}(t)$ decreases favoring an increase of $E_F(t)$ and $E_B(t)$ such

that $E_F(t) \ll E_B(t)$. Recall that in this time interval $\rho_F^{(1)}(x;t)$ breaks into two repelling density branches [Fig. 4 (h)]. As a consequence the increase of $E_F(t)$ can be attributed to the increasing kinetic energy of the fermions, in this time interval, that leads to a transfer of energy from the fermions to the bosons. For $t > 10$, $E_B(t)$ exhibits an overall increasing tendency oscillating out-of-phase with $E_{BF}(t)$ which in turn decreases. Simultaneously, $E_F(t)$ slightly increases in time. This approximately constant behavior of $E_F(t)$ essentially reflects the almost steady behavior of $\rho_F^{(1)}(x;t)$ during evolution [see also Fig. 4 (h)]. Another important observation here is that $E_B(t)$ is found to be larger for $g_{BF} = 3$ when compared to the relevant energy contribution for $g_{BF} = 1.5$, indicating that for these stronger interspecies interactions the energy gain of the bosonic bath is even larger.

F. Degree of correlations

To quantify the correlated nature of the BF mixture dynamics we next estimate the degree of entanglement (interspecies correlations) by employing $S_{VN}(t)$ [Eq. (9)]. Additionally, we invoke $F_\sigma(t)$ [Eq. (10)] to infer about the fragmentation (intraspecies correlations) of the system's MB state [Eqs. (2) and (3)]. Recall that $S_{VN}(t) \neq 0$ designates the presence of entanglement otherwise the system is termed non-entangled [80, 88]. Also, when $F_\sigma(t) > 0$ the σ -species is said to be intraspecies correlated (see also Sec. II C). Most importantly, since the fermionic species consist of spin-polarized, namely non-interacting, fermions the existence of their intraspecies correlations during evolution is caused by the presence of the interspecies correlations.

Figure 9 presents $S_{VN}(t)$ and $F_\sigma(t)$ during the interspecies interaction quench dynamics of the BF mixture for a varying g_{BF} . Recall that the initial (ground state) single-particle densities of the σ species [see the discussion in Sec. III A] are almost identical within the MF and the MB description [Figs. 1 (a), (d)]. As a result at $t = 0$ the BF mixture is mainly uncorrelated and this is also confirmed by the fact that $S_{VN}(0) \approx 0$, $F_F(0) \approx 0$ and $F_B(0) \approx 0.02$ [see Fig. 9]. On the other hand, inspecting the time-evolution of the above-mentioned quantities we can infer about the presence of both inter- and interspecies correlations. For weak postquench interactions, $g_{BF} = 0.3$, there is only a small amount of inter- and intraspecies correlations since both $S_{VN}(t)$ and $F_\sigma(t)$ are suppressed taking very small values and being almost constant in time. However, for stronger interactions such as $g_{BF} = 1.5, 3$ the entropy $S_{VN}(t)$ as well as $F_\sigma(t)$ increase during the evolution and tend to saturate to a certain finite value. This indicates that the underlying MB state is strongly both entangled and fragmented. Also stronger postquench effective interspecies interactions, g_{BF} , result to larger values of $S_{VN}(t)$ and $F_\sigma(t)$. Another interesting observation is that $S_{VN}(t)$

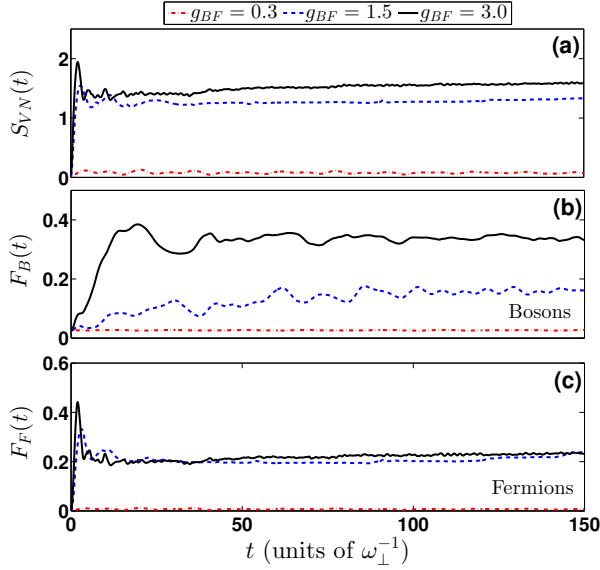


FIG. 9. (a) Von-Neumann entropy for fixed $g_{BB} = 0.5$ and different postquench g_{BF} (see legend). (b) Deviation from unity of the first natural population of the bosonic cloud for $g_{BB} = 0.5$ and varying g_{BF} . (c) Deviation from unity of the first two natural populations of the fermions for $g_{BB} = 0.5$ and distinct g_{BF} (see legend). Other system parameters are the same as in Fig. 2.

and $F_F(t)$ increase more rapidly at the initial stages of the dynamics than $F_B(t)$ which grows in a slower manner. This indicates that the interspecies correlations and fermionic intraspecies correlations are stronger than the bosonic intraspecies ones (see also below).

Moreover, we can infer that for strong postquench interactions, e.g. $g_{BF} = 1.5$, all the above-described correlation measures show a tendency to saturation for times $t > 80$. Indeed by inspecting the dynamics of the corresponding natural species populations $\lambda_k(t)$ with $k = 1, 2, \dots, 10$ as well as the natural populations of the orbitals of each species, namely $n_i^B(t)$ ($i = 1, 2, 3$) and $n_i^F(t)$ ($i = 1, 2, \dots, 8$), we observe that they rapidly oscillate for $t < 80$ while at later times a slower small amplitude redistribution takes place (results not shown here for brevity). This slow redistribution of $\lambda_k(t)$, $n_i^B(t)$, and $n_i^F(t)$ is essentially imprinted in $S_{VN}(t)$, $F_B(t)$ and $F_F(t)$ respectively and it is reminiscent of a prethermalization phenomenon [89] occurring at the individual correlation levels [90, 91]. Recall that such a saturation behavior occurs also for other observables, e.g. the relative distance between the two fermions for $g_{BF} = 3$ [Fig. 7], further supporting the tendency of the system to prethermalize. However in order to strictly infer about the occurrence of prethermalization dynamics requires a further investigation and an in-depth analysis. More specifically, one needs to compare e.g. with the predictions of the corresponding Gaussian orthogonal ensemble of random matrices, and also monitor the time-evolution of the system for longer evolution times, an investigation which cer-

tainly lies beyond the scope of the present effort.

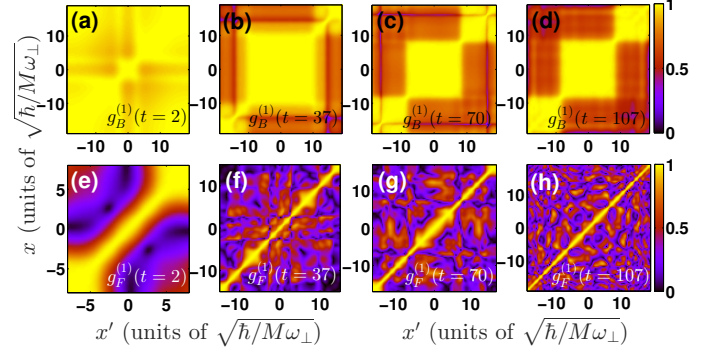


FIG. 10. (a)-(d) Snapshots of the one-body coherence function at different time instants (see legends) of the evolution following an interspecies interaction quench from $g_{BF} = 0.1$ to $g_{BF} = 1.5$. (e)-(h) The same as before but for the fermions. The remaining system parameters are the same as in Fig. 4.

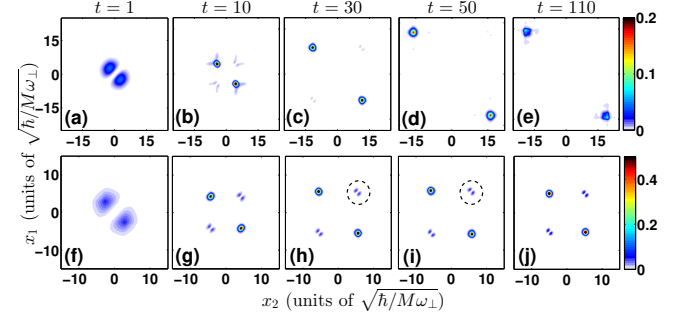


FIG. 11. (a)-(d) The fermionic two-body reduced density matrix at different time instants (see legends) of the evolution upon considering an interspecies interaction quench from $g_{BF} = 0.1$ to (a)-(e) $g_{BF} = 1.5$ and (f)-(j) $g_{BF} = 3$. The dashed circles in (h), (i) indicate the population close to the diagonal elements for $x_1, x_2 > 0$. The remaining system parameters are the same as in Fig. 4.

G. Evolution of the one-body coherence

In order to further expose the role of correlations in the above-discussed interaction quench dynamics of the BF mixture we finally resort to the corresponding σ species one-body coherence function $g_{\sigma}^{(1)}(x, x'; t)$ of Eq. (7) [see Fig. 10]. Closely inspecting $g_B^{(1)}(x, x'; t)$ we can deduce that the bosonic species is fully coherent within the time interval ($0 < t < 50$) that the two fermionic density branches travel towards its edges [see also Figs. 4 (e), (g)]. Indeed, for this time interval $g_B^{(1)}(x, x'; t) \approx 1$ for every x, x' lying within the spatial extent of the bosonic cloud [Figs. 10 (a), (b)]. For later evolution times where the aforementioned fermionic density branches probe the edges of the bosonic species we observe that losses of coherence, namely $g_B^{(1)}(x, x'; t) < 1$, occur either between

the two edges, e.g. $10 < x' < 15$ and $-15 < x < -10$, or between one edge and the core of the bosonic cloud, e.g. $-8 < x' < 8$ and $10 < x < 15$. Regarding the coherence of the impurity species we can infer that each fermionic density branch is perfectly coherent with itself having $g_A^{(1)}(x, x'; t) \approx 1$ [Figs. 10 (e)-(h)] but it is almost fully incoherent with the other branch, since e.g. $g_A^{(1)}(x = 8, x' = -8; t) \approx 0.3$ throughout the dynamics [Figs. 10 (g)-(h)]. Therefore we can conclude that during the evolution the BF mixture develops Mott-like one-body correlations [80, 88, 92] that emerge between the two fermionic density branches indicating their spatial localization.

H. Dynamics of the two-body reduced density matrix

Another interesting prospect is to unravel the spatially resolved dynamics of the two fermionic impurities with respect to one another. Note that the impurities are dressed by the excitations of the bosonic gas forming quasiparticles. In turn, these quasiparticles can move independently or interact thereby possibly forming a bound state in the latter case. To track the underlying two particle dynamics we invoke the time-evolution of the corresponding diagonal of the two-body fermionic reduced density matrix

$$\rho_{FF}^{(2)}(x_1, x_2; t) = \langle \Psi_{MB}(t) | \hat{\Psi}^{F\dagger}(x_1) \hat{\Psi}^{F\dagger}(x_2) \times \hat{\Psi}^F(x_1) \hat{\Psi}^F(x_2) | \Psi_{MB}(t) \rangle. \quad (12)$$

Here, $\hat{\Psi}^F(x_1)$ denotes the fermionic field operator that annihilates a fermion at position x_1 . Recall that the diagonal of the two-body reduced density matrix provides the probability of measuring simultaneously one fermion at location x_1 and the other at x_2 [80, 81, 107]. The dynamics of $\rho_{FF}^{(2)}(x_1, x_2; t)$ at specific time-instants is presented in Fig. 11 when following an interspecies interaction quench from $g_{BF} = 0.1$ to $g_{BF} = 1.5$ [Figs. 11 (a)-(e)] and $g_{BF} = 3$ [Figs. 11 (f)-(j)]. Referring to $g_{BF} = 1.5$, we observe that initially [Fig. 11 (a)] the two fermions reside close to the trap center with one of them located in the vicinity of $0 < x_1 < 5$ and the other at $-5 < x_2 < 0$ as shown by the populated anti-diagonal elements of $\rho_{FF}^{(2)}(x_1, x_2; t)$. The existence of a correlation hole occurring in the diagonal of $\rho_{FF}^{(2)}(x_1, x_2 = x_1; t)$ throughout the evolution is, of course, a consequence of Pauli's exclusion principle. At the early stages of the dynamics [Fig. 11 (b)] the two fermions move in the opposite direction with respect to one another, while as time evolves their distance becomes larger, see Figs. 11 (c)-(e). This increase of their relative distance has already been discussed in Section IIID and visualized in Fig. 7 (b). Therefore each fermion resides in one of the density branches emerging in $\rho_F^{(1)}(x; t)$ [Fig. 4 (g)]. As a consequence we can infer the formation of two largely indepen-

dent quasiparticles. Note here that these quasiparticles are located well inside the bosonic gas until $t \approx 60$, while for later times reside at the edges of the Thomas-Fermi radius of the BEC [see also Fig. 4 (g)] and are held at this location by the external harmonic trap. Such an independent fermionic quasiparticle formation has already been reported in [114].

Turning to very strong postquench interactions, i.e. $g_{BF} = 3$, we observe an overall same phenomenology as before but most importantly in this case there is also a non-negligible population of the $\rho_{FF}^{(2)}(x_1, x_2; t)$ elements close to its diagonal, e.g. see the dashed circles in Figs. 11 (h), (i). The latter contribution indicates an additional emergent attractive tendency between the two fermions and it is suggestive of the formation of a bound state between them. In particular, at short evolution times [Fig. 11 (f)] the two fermions are well separated residing one at $0 < x_1 < 5$ and the other at $-5 < x_2 < 0$, see the anti-diagonal elements of $\rho_{FF}^{(2)}(x_1, x_2; t)$. As time evolves we observe that the two fermions can be essentially in two different two-body configurations (see below). Namely, either the two fermions remain spatially separated throughout the dynamics [see the anti-diagonal elements of $\rho_{FF}^{(2)}(x_1, x_2; t)$] or they are very close to each other [see the diagonal elements of $\rho_{FF}^{(2)}(x_1, x_2; t)$] which is reminiscent of the formation of a bound state between them. Notice also that the occurrence of this latter two-body configuration is also responsible for the emergent attraction between the two density branches appearing in the corresponding fermionic single-particle density evolution [Fig. 4 (h)]. Similar bound state formation has been discussed in the context of bosonic impurities [114–116]. The appearance of these two different two-body configurations can be understood by resorting to the spectral decomposition of the two-body density matrix. The latter reads $\rho_{FF}^{(2)}(x_1, x_2; t) = \sum_{i=1}^{d_F^2} \lambda_i^{(2)}(t) \alpha_i^{(2)}(x_1, x_2; t) \alpha_i^{(2)*}(x_1, x_2; t)$, where $\lambda_i^{(2)}(t)$ and $\alpha_i^{(2)}(x_1, x_2; t)$ are the eigenvalues and eigenfunctions (also known as natural geminals) of $\rho_{FF}^{(2)}(x_1, x_2; t)$ respectively. Indeed, inspecting the individual contributions of $\alpha_i^{(2)}(x_1, x_2; t)$, $i = 1, 2, \dots$, we can deduce that the state of the well-separated quasiparticles is described by $\alpha_1^{(2)}(x_1, x_2; t)$ whilst the existence of the bound state is caused by the higher-order contributions namely $\alpha_i^{(2)}(x_1, x_2; t)$ with $i > 1$ (results not shown here for brevity).

IV. SUMMARY AND CONCLUSIONS

We have investigated the nonequilibrium quantum dynamics of a harmonically trapped particle imbalanced BF mixture consisting of two spin-polarized fermionic impurities and a majority bosonic species upon quenching the interspecies repulsion from weak to larger values. Comparing the dynamics within the MF approximation and

the MB level enables us to expose the crucial role of correlations, especially in the time-evolution of the impurities, and reveal a variety of dynamical regimes occurring for different interspecies interaction strengths.

In the ground state of the particle imbalanced BF mixture a phase separation between the two species occurs, both at the MF and the MB level for increasing interspecies interaction strengths which overcome the bosonic intraspecies ones. In particular, the fermionic ground state single-particle density deforms from a Gaussian-like distribution located around the trap center and fully overlapping with the Thomas-Fermi profile of the bosonic species into two spatially separated density humps residing at the edges of this Thomas-Fermi profile. To trigger the dynamics we consider an interspecies interaction quench from weak towards larger repulsions. Depending on the final value of the interspecies interactions we realize four different dynamical regimes. For weak postquench interactions both species undergo a breathing motion while remaining miscible throughout the evolution. Here, the degree of correlations is negligible and therefore the MF approximation adequately captures the dynamics of the mixture. Increasing the postquench interaction strength the density of the impurities splits into two repelling density peaks moving towards the edges of the bosonic cloud which performs a breathing motion. In the MF approximation, these density branches reach the edges of the bosonic cloud and then they are reflected back to the trap center where they collide and subsequently exhibit a dispersive behavior. The latter suggests that the impurities are in a superposition of several lower-lying excited states of their external potential. At the MB level the dynamics of the mixture shows the same overall phenomenology. However, the dispersive character of the single-particle density of the impurities is more pronounced, indicating that they are in a superposition of higher excited states compared to the MF case.

For stronger postquench interaction strengths the dynamical behavior of both the fermionic and the bosonic species alters drastically. Within the MF approximation we observe the spontaneous generation of two DB soliton states, with the bright solitary waves building upon the fermionic species and the corresponding dark states appearing in the bosonic gas. We have verified their existence by inspecting the phase jump of the dark solitons as well as by performing a fitting of the numerically obtained single-particle densities to the analytical waveforms of this type of states. Turning to the MB approach we identify significant deviations with respect to the MF dynamics. In particular, after the quench the fermionic density breaks into two distinct localized humps which travel towards the edges of the bosonic cloud and are accompanied by the formation of density dips in the latter resembling this way DB states. For later times, the fermionic density humps reach the edges of the bosonic cloud and undergo a small amplitude oscillatory motion around the Thomas-Fermi radius of the bosonic species. This latter process signifies the dynamical decay of the

DB state and thus provides an undeniable effect of the presence of correlations.

Quenching to very strong interspecies interactions and focusing on the MF approximation we again observe the formation of DB states with a slightly modified oscillation period and amplitude of the bright states when compared to weaker interspecies interactions. However, at the MB level the fermionic density initially splits into two repelling humps which subsequently oscillate with a very small amplitude and deeper in the evolution tend to approach an almost steady state. Here, the majority species forms density dips at the spatial regions where the density peaks of the impurities density are located.

To further understand the dynamics we have employed other diagnostics such as the different energy contributions of each of the species as well as their mutual interaction energy and the one-body coherence function. Inspecting the energy contributions during the dynamics it becomes evident that entering the strong interspecies interaction regime after the quench an energy exchange process from the impurities to the bosonic bath occurs when correlations are taken into account. However, within the MF approximation a periodic back and forth energy transfer from the bright states (impurities) to the BEC medium takes place. Monitoring the one-body coherence function reveals the appearance of Mott-like correlations between the emergent fermionic density humps for strong postquench interactions, thus indicating their tendency for localization. Moreover, examining the time-evolution of the fermionic two-body reduced density matrix unveils that depending on the strength of the postquench repulsion the two fermions either behave almost independently or experience a weak attraction for very strong interspecies couplings. Finally, resorting to the population eigenvalues of the single-particle functions appearing in the MB ansatz we have identified that both inter- and intraspecies correlations become stronger for a larger postquench interaction strength.

There is a multitude of several promising extensions of the current work that are of interest for future investigations. An interesting prospect is to unravel the corresponding interspecies interaction quench dynamics in the case of two interacting bosonic impurities immersed in either a bosonic or fermionic bath in order to systematically examine the role of their induced interactions in the course of the evolution. Also, the inclusion of temperature effects in such an investigation would be highly desirable [117, 118]. Another intriguing direction would be to examine the periodically driven dynamics of one and two impurities inside a non-perturbed bosonic bath and subsequently inspect their emergent dissipative motion into the bath with respect to the driving frequency. Certainly the simulation of the corresponding radiofrequency spectrum [63] or the structure factor of the present system [77] by considering spinor impurities in order to identify the emerging polaronic states and subsequently investigate their lifetime and residue constitutes an intriguing perspective.

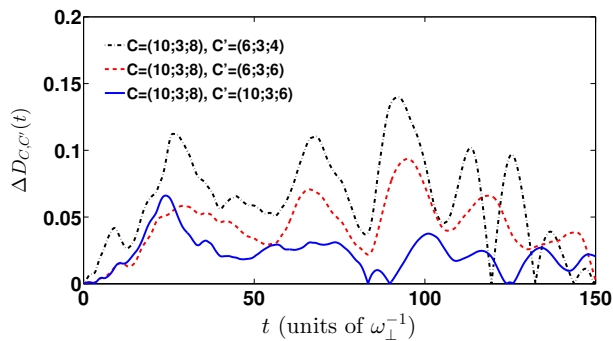


FIG. 12. Time-evolution of the deviation $\Delta D_{C,C'}(t)$ of the relative distance among the two fermionic impurities between the $C = (10; 3; 8)$ and other orbital configurations $C = (D; d_A; d_B)$ (see legend). The harmonically trapped BF mixture consists of $N_B = 100$ bosons and $N_F = 2$ fermions and it is prepared in its ground state with $g_{BB} = 0.5$ and $g_{BF} = 0.1$. To trigger the dynamics we follow an interspecies interaction quench to $g_{BF} = 1.5$.

Appendix A: Convergence and ingredients of the many-body simulations

As we have already discussed in the main text, in order to simulate the correlated nonequilibrium dynamics of the considered Bose-Fermi mixture we utilize the Multi-Layer Multi-Configurational Time-Dependent Hartree Method for Atomic Mixtures (ML-MCTDHX) [82]. It is a variational method for solving the time-dependent MB Schrödinger equation of various types of atomic mixtures consisting either of bosonic [66, 80] or fermionic [81, 106, 107] species and also spin degrees of freedom [63, 77]. The key ingredient of this numerical approach is the expansion of the MB wavefunction with respect to a time-dependent variationally optimized basis. This allows us to include all the relevant intra- and interspecies correlations into our MB ansatz using a computationally feasible basis size. Therefore the relevant subspace of the Hilbert space at each time instant of the evolution is chosen in a more efficient manner when compared to methods relying on a time-independent basis.

In particular, the considered Hilbert space truncation is designated by the employed orbital configuration space denoted as $C = (D; d_B; d_F)$. Here, $D = D_B = D_F$ and d_B, d_F refer to the number of species and single-particle functions respectively of each species [see also Eqs. (2) and (3)]. Also, within our numerical calculations we use

a primitive basis based on a sine discrete variable representation including 600 grid points. We note that this sine discrete variable representation intrinsically introduces hard-wall boundary conditions which in our case are imposed at $x_{\pm} = \pm 50$ and, of course, do not affect our results since we do not observe appreciable densities to occur beyond $x_{\pm} = \pm 25$. To infer about the convergence of the MB simulations we testify that the observables of interest become almost insensitive (within a given level of accuracy) upon varying the used orbital configuration space, $C = (D; d_A; d_B)$. Note also that all MB calculations presented in the main text are based on the orbital configuration $C = (10; 3; 8)$. To showcase the convergence of our results for a varying number of species and single-particle functions e.g. we track the relative distance between the two fermionic impurities during the nonequilibrium dynamics. More precisely, we calculate its absolute deviation between the $C = (10; 3; 8)$ and other orbitals configurations $C' = (D; d_A; d_B)$

$$\Delta D_{C,C'}(t) = \frac{|D_C(t) - D_{C'}(t)|}{D_C(t)}. \quad (\text{A1})$$

Figure 12 shows $\Delta D_{C,C'}(t)$ between the two fermionic impurities upon considering an interspecies interaction quench from $g_{BF} = 0.1$ to $g_{BF} = 1.5$. It becomes evident that a systematic convergence of $\Delta D_{C,C'}(t)$ is achieved. For instance, comparing $\Delta D_{C,C'}(t)$ between the $C = (10; 3; 8)$ and $C' = (6; 3; 6)$ orbital configurations we deduce that the corresponding relative difference lies below 9% throughout the evolution. Also, the relative deviation, $\Delta D_{C,C'}(t)$, when $C = (10; 3; 8)$ and $C' = (10; 3; 6)$ becomes at most of the order of 6% in the course of the dynamics. Finally, we remark that a similar analysis has been performed for all other postquench interspecies interaction strengths presented in the main text and found to be adequately converged (not shown here for brevity).

ACKNOWLEDGEMENTS

S.I.M. and P.S. gratefully acknowledge financial support by the Deutsche Forschungsgemeinschaft (DFG) in the framework of the SFB 925 “Light induced dynamics and control of correlated quantum systems”. S.I.M thanks A. G. Volosniev for illuminating discussions regarding the polaron problem.

[1] C. Chin, R. Grimm, P. Julienne, and E. Tiesinga, Rev. Mod. Phys. **82**, 1225 (2010).
 [2] T. Köhler, K. Góral, and P. S. Julienne, Rev. Mod. Phys. **78**, 1311 (2006).
 [3] G. Modugno, M. Modugno, F. Riboli, G. Roati, and M. Inguscio, Phys. Rev. Lett. **89**, 190404 (2002).

[4] C. J. Myatt, E. A. Burt, R. W. Ghrist, E. A. Cornell, and C. E. Wieman, Phys. Rev. Lett. **78**, 586 (1997).
 [5] J. Stenger, S. Inouye, D. M. Stamper-Kurn, H.-J. Miesner, A. P. Chikkatur, and W. Ketterle, Nature (London) **396**, 345 (1998).

- [6] C.-H. Wu, J. W. Park, P. Ahmadi, S. Will, and M. W. Zwierlein, *Phys. Rev. Lett.* **109**, 085301 (2012).
- [7] M.-S. Heo, T. T. Wang, C. A. Christensen, T. M. Rvachov, D. A. Cotta, J.-H. Choi, Y.-R. Lee, and W. Ketterle, *Phys. Rev. A* **86**, 021602 (2012).
- [8] T. D. Cumby, R. A. Shewmon, M.-G. Hu, J. D. Perreault, and D. S. Jin, *Phys. Rev. A* **87**, 012703 (2013).
- [9] G. Roati, M. Zaccanti, C. D'Errico, J. Catani, M. Modugno, A. Simoni, M. Inguscio, and G. Modugno, *Phys. Rev. Lett.* **99**, 010403 (2007).
- [10] K. Pilch, A. D. Lange, A. Prantner, G. Kerner, F. Ferlaino, H.-C. Nägerl, and R. Grimm, *Phys. Rev. A* **79**, 042718 (2009).
- [11] A. Schirotzek, C.-H. Wu, A. Sommer, and M. W. Zwierlein, *Phys. Rev. Lett.* **102**, 230402 (2009).
- [12] C. Kohstall, M. Zaccanti, M. Jag, A. Trenkwalder, P. Massignan, G. M. Bruun, F. Schreck, and R. Grimm, *Nature* **485**, 615 (2012).
- [13] M. Koschorreck, D. Pertot, E. Vogt, B. Fröhlich, M. Feld, and M. Köhl, *Nature* **485**, 619 (2012).
- [14] Y. Zhang, W. Ong, I. Arakelyan, and J. E. Thomas, *Phys. Rev. Lett.* **108**, 235302 (2012).
- [15] N. Spethmann, F. Kindermann, S. John, C. Weber, D. Meschede, and A. Widera, *Phys. Rev. Lett.* **109**, 235301 (2012).
- [16] F. Scazza, G. Valtolina, P. Massignan, A. Recati, A. Amico, A. Burchianti, C. Fort, M. Inguscio, M. Zaccanti, and G. Roati, *Phys. Rev. Lett.* **118**, 083602 (2017).
- [17] N. J. Robinson, J. S. Caux, and R. M. Konik, *Phys. Rev. Lett.* **116**, 145302 (2016).
- [18] M. E. Gershenson, V. Podzorov, and A. F. Morpurgo, *Rev. Mod. Phys.* **78**, 973 (2006).
- [19] E. Dagotto, *Rev. Mod. Phys.* **66**, 763 (1994).
- [20] J. Koepsell, J. Vijayan, P. Sompet, F. Grusdt, T. A. Hilker, E. Demler, G. Salomon, I. Bloch and C. Gross, *Nature* **572**, 358 (2019).
- [21] J. Bardeen, G. Baym, and D. Pines, *Phys. Rev.* **156**, 207 (1967).
- [22] G. Baym, and C. Pethick, *Landau Fermi-Liquid Theory: Concepts and Applications* (Wiley-VCH, 1991).
- [23] S. Nascimbène, N. Navon, K. J. Jiang, L. Tarruell, M. Teichmann, J. McKeever, F. Chevy, and C. Salomon, *Phys. Rev. Lett.* **103**, 170402 (2009).
- [24] M. Punk, P. T. Dumitrescu, and W. Zwerger, *Phys. Rev. A* **80**, 053605 (2009).
- [25] F. Chevy, and C. Mora, *Rep. Prog. Phys.* **73**, 112401 (2010).
- [26] X. Cui, and H. Zhai, *Phys. Rev. A* **81**, 041602(R) (2010).
- [27] S. Pilati, G. Bertaina, S. Giorgini, and M. Troyer, *Phys. Rev. Lett.* **105**, 030405 (2010).
- [28] P. Massignan, and G. Bruun, *Eur. Phys. J. D* **65**, 83 (2011).
- [29] R. Schmidt, and T. Enss, *Phys. Rev. A* **83**, 063620 (2011).
- [30] R. Schmidt, T. Enss, V. Pietilä, and E. Demler, *Phys. Rev. A* **85**, 021602 (2012).
- [31] V. Ngampruetikorn, J. Levinsen, and M. M. Parish, *Europhys. Lett.* **98**, 30005 (2012).
- [32] P. Massignan, Z. Yu, and G. M. Bruun, *Phys. Rev. Lett.* **110**, 230401 (2013).
- [33] P. Massignan, M. Zaccanti, and G. M. Bruun, *Rep. Prog. Phys.* **77**, 034401 (2014).
- [34] R. Schmidt, M. Knap, D. A. Ivanov, J. -S. You, M. Cetina, and E. Demler, *Rep. Prog. Phys.* **81**, 024401 (2018).
- [35] E. Burovski, V. Cheianov, O. Gamayun, and O. Lychkovskiy, *Phys. Rev. A* **89**, 041601 (2014).
- [36] O. Gamayun, O. Lychkovskiy, E. Burovski, M. Malcolmson, V. V. Cheianov, and M. B. Zvonarev, *Phys. Rev. Lett.* **120**, 220605 (2018).
- [37] S. Palzer, C. Zipkes, C. Sias, and M. Köhl, *Phys. Rev. Lett.* **103**, 150601 (2009).
- [38] J. Tempere, W. Casteels, M. K. Oberthaler, S. Knoop, E. Timmermans, and J. T. Devreese, *Phys. Rev. B* **80**, 184504 (2009).
- [39] T. Fukuhara, A. Kantian, M. Endres, M. Cheneau, P. Schauss, S. Hild, D. Bellem, U. Schollwöck, T. Giamarchi, C. Gross, I. Bloch, and S. Kuhr, *Nat. Phys.* **9**, 235 (2013).
- [40] R. Scelle, T. Rentrop, A. Trautmann, T. Schuster, and M. K. Oberthaler, *Phys. Rev. Lett.* **111**, 070401 (2013).
- [41] R. Schmidt, H. R. Sadeghpour, and E. Demler, *Phys. Rev. Lett.* **116**, 105302 (2016).
- [42] L. A. Peña Ardila, and S. Giorgini, *Phys. Rev. A* **94**, 063640 (2016).
- [43] L. A. Ardila, N. B. Jørgensen, T. Pohl, S. Giorgini, G. M. Bruun, and J. J. Arlt, *Phys. Rev. A* **99**, 063607 (2019).
- [44] F. Grusdt, R. Schmidt, Y. E. Shchadilova, and E. Demler, *Phys. Rev. A* **96**, 013607 (2017).
- [45] A. G. Volosniev, and H.-W. Hammer, *Phys. Rev. A* **96**, 031601 (2017).
- [46] N. E. Guenther, P. Massignan, M. Lewenstein, and G. M. Bruun, *Phys. Rev. Lett.* **120**, 050405 (2018).
- [47] D. Mayer, F. Schmidt, D. Adam, S. Haupt, J. Koch, T. Lausch, J. Nettersheim, Q. Bouton, and A. Widera, *J. Phys. B: At. Mol. and Opt. Phys.* **52**, 015301 (2018).
- [48] J. Catani, G. Lamporesi, D. Naik, M. Gring, M. Inguscio, F. Minardi, A. Kantian, and T. Giamarchi, *Phys. Rev. A* **85**, 023623 (2012).
- [49] G. E. Astrakharchik, and L. P. Pitaevskii, *Phys. Rev. A* **70**, 013608 (2004).
- [50] F. M. Cucchietti, and E. Timmermans, *Phys. Rev. Lett.* **96**, 210401 (2006).
- [51] R. M. Kalas, and D. Blumme, *Phys. Rev. A* **73**, 043608 (2006).
- [52] M. Bruderer, A. Klein, S. R. Clark, and D. Jaksch, *Europhys. Lett.* **82**, 30004 (2008).
- [53] K. Sacha, and E. Timmermans, *Phys. Rev. A* **73**, 063604 (2006).
- [54] M. Bruderer, A. Klein, S. R. Clark, and D. Jaksch, *Phys. Rev. A* **76**, 011605(R) (2007).
- [55] A. Privitera, and W. Hofstetter, *Phys. Rev. A* **82**, 063614 (2010).
- [56] W. Casteels, J. Tempere, and J. T. Devreese, *Phys. Rev. A* **86**, 043614 (2012).
- [57] W. Casteels, J. Tempere, and J. T. Devreese, *Phys. Rev. A* **88**, 013613 (2013).
- [58] B. Kain, and H. Y. Ling, *Phys. Rev. A* **94**, 013621 (2016).
- [59] N. B. Jørgensen, L. Wacker, K. T. Skalmstang, M. M. Parish, J. Levinsen, R. S. Christensen, G. M. Bruun, and J. J. Arlt, *Phys. Rev. Lett.* **117**, 055302 (2016).
- [60] M.-G. Hu, M. J. Van de Graaff, D. Kedar, J. P. Corson, E. A. Cornell, and D. S. Jin, *Phys. Rev. Lett.* **117**, 055301 (2016).

- [61] J. Catani, G. Barontini, G. Lamporesi, F. Rabatti, G. Thalhammer, F. Minardi, S. Stringari, and M. Inguscio, *Phys. Rev. Lett.* **103**, 140401 (2009).
- [62] Z. Z. Yan, Y. Ni, C. Robens, and M. W. Zwierlein, arXiv:**1904.02685** (2019).
- [63] S. I. Mistakidis, G. C. Katsimiga, G. M. Koutentakis, and P. Schmelcher, *New J. Phys.* **21**, 043032 (2019).
- [64] F. Grusdt, K. Seetharam, Y. Shchadilova, and E. Demler, *Phys. Rev. A* **97**, 033612 (2018).
- [65] S. I. Mistakidis, F. Grusdt, G. M. Koutentakis, and P. Schmelcher, arXiv:**1907.06196** (2019).
- [66] S. I. Mistakidis, A. G. Volosniev, N. T. Zinner, and P. Schmelcher, *Phys. Rev. A* **100**, 013619 (2019).
- [67] M. Drescher, M. Salmhofer, and T. Enss, *Phys. Rev. A* **99**, 023601 (2019).
- [68] W. Li, and S. Das Sarma, *Phys. Rev. A* **90**, 013618 (2014).
- [69] L. A. Peña Ardila, and S. Giorgini, *Phys. Rev. A* **92**, 033612 (2015).
- [70] Y. E. Shchadilova, R. Schmidt, F. Grusdt, and E. Demler, *Phys. Rev. Lett.* **117**, 113002 (2016).
- [71] S. P. Rath, and R. Schmidt, *Phys. Rev. A* **88**, 053632 (2013).
- [72] F. Grusdt, G. E. Astrakharchik, and E. Demler, *New J. Phys.* **19**, 103035 (2017).
- [73] X. Li, G. Bighin, E. Yakaboylu, and M. Lemeshko, *Mol. Phys.* 1-8 (2019).
- [74] B. Kain, and H. Y. Ling, *Phys. Rev. A* **98**, 033610 (2018).
- [75] C.J. Pethick, and H. Smith, *Bose-Einstein condensation in dilute gases*. Cambridge University Press 2002.
- [76] M. Lewenstein, A. Sanpera, and V. Ahufinger, *Ultracold Atoms in Optical Lattices: Simulating Quantum Many-body Systems* (Oxford University Press, Oxford, 2012).
- [77] S. I. Mistakidis, G. C. Katsimiga, G. M. Koutentakis, T. Busch, and P. Schmelcher, *Phys. Rev. Lett.* **122**, 183001 (2019).
- [78] M. Tylutki, A. Recati, F. Dalfovo, and S. Stringari, *New J. Phys.* **18**, 053014 (2016).
- [79] T. Karpiuk, M. Brewczyk, S. Ospelkaus-Schwarzer, K. Bongs, M. Gajda, and K. Rzaewski, *Phys. Rev. Lett.* **93**, 100401 (2004).
- [80] S. I. Mistakidis, G. C. Katsimiga, P. G. Kevrekidis, and P. Schmelcher, *New J. Phys.* **20**, 043052 (2018).
- [81] J. Erdmann, S. I. Mistakidis, and P. Schmelcher, *Phys. Rev. A* **99**, 013605 (2019).
- [82] L. Cao, V. Bolsinger, S. I. Mistakidis, G. M. Koutentakis, S. Krönke, J. M. Schurer, and P. Schmelcher, *J. Chem. Phys.* **147**, 044106 (2017).
- [83] R. S. Lous, I. Fritsche, M. Jag, F. Lehmann, E. Kirilov, B. Huang, and R. Grimm, *Phys. Rev. Lett.* **120**, 243403 (2018).
- [84] R. Roth, *Phys. Rev. A* **66**, 013614 (2002).
- [85] L. Viverit, C. J. Pethick, and H. Smith, *Phys. Rev. A* **61**, 053605 (2000).
- [86] P. Siegl, S. I. Mistakidis, and P. Schmelcher, *Phys. Rev. A* **97**, 053626 (2018).
- [87] B. Huang, I. Fritsche, R. S. Lous, C. Baroni, J. Walraven, E. Kirilov, and R. Grimm, arXiv:**1812.06445** (2018).
- [88] G. C. Katsimiga, G. M. Koutentakis, S. I. Mistakidis, P. G. Kevrekidis, and P. Schmelcher, *New J. Phys.* **19**, 073004 (2017).
- [89] F. H. Essler, and M. Fagotti, *J. Stat. Mech. Theory and Experiment*, **6**, 064002 (2016).
- [90] A. U. Lode, B. Chakrabarti, and V. K. Kota, *Phys. Rev. A* **92**, 033622 (2015).
- [91] S. Bera, S. K. Haldar, B. Chakrabarti, A. Trombettoni, and V. K. B. Kota, arXiv:**1905.01075** (2019).
- [92] J. F. Sherson, C. Weitenberg, M. Endres, M. Cheneau, I. Bloch, and S. Kuhr, *Nature (London)* **467**, 68 (2010).
- [93] E.V. Kempen, B. Marcellis, and S.J.J.M.F. Kokkelmans, *Phys. Rev. A* **70**, 050701 (2004).
- [94] K. Honda, Y. Takasu, T. Kuwamoto, M. Kumakura, Y. Takahashi, and T. Yabuzaki, *Phys. Rev. A* **66**, 021401 (2002).
- [95] Y. Takasu, K. Maki, K. Komori, T. Takano, K. Honda, M. Kumakura, T. Yabuzaki, and Y. Takahashi, *Phys. Rev. Lett.* **91**, 040404 (2003).
- [96] M. Olshanii, *Phys. Rev. Lett.* **81**, 938 (1998).
- [97] P. Ao, and S. T. Chui, *Phys. Rev. A* **58**, 4836 (1998).
- [98] R. Horodecki, P. Horodecki, M. Horodecki, and K. Horodecki, *Rev. Mod. Phys.* **81**, 865 (2009).
- [99] M. Roncaglia, A. Montorsi, and M. Genovese, *Phys. Rev. A* **90**, 062303 (2014).
- [100] L. Cao, S. Krönke, O. Vendrell, and P. Schmelcher, *J. Chem. Phys.* **139**, 134103 (2013).
- [101] J. Frenkel, in *Wave Mechanics* 1st ed. (Clarendon Press, Oxford, 1934), pp. 423-428.
- [102] P. A. Dirac, *Proc. Camb. Phil. Soc.* **26**, 376, Cambridge University Press (1930).
- [103] M. Naraschewski, and R. J. Glauber, *Phys. Rev. A* **59**, 4595 (1999).
- [104] K. Sakmann, A. I. Streltsov, O. E. Alon, and L. S. Cederbaum, *Phys. Rev. A* **78**, 023615 (2008).
- [105] A. Bergschneider, V. M. Klinkhamer, J. H. Becher, R. Klemt, G. Zürn, P. M. Preiss, and S. Jochim, *Phys. Rev. A* **97**, 063613 (2018).
- [106] G. M. Koutentakis, S. I. Mistakidis, and P. Schmelcher, *New J. Phys.* **21**, 053005 (2019).
- [107] J. Erdmann, S. I. Mistakidis, and P. Schmelcher, *Phys. Rev. A* **98**, 053614 (2018).
- [108] H. Kiehn, S. I. Mistakidis, G. C. Katsimiga, and P. Schmelcher, *Phys. Rev. A* **100**, 023613 (2019).
- [109] D. Yan, J. J. Chang, C. Hamner, P. G. Kevrekidis, P. Engels, V. Achilleos, D. J. Frantzeskakis, R. Carretero-González and P. Schmelcher, *Phys. Rev. A* **84**, 053630 (2011).
- [110] G. C. Katsimiga, J. Stockhofe, P. G. Kevrekidis, and P. Schmelcher, *Phys. Rev. A* **95**, 013621 (2017).
- [111] G. C. Katsimiga, P. G. Kevrekidis, B. Prinari, G. Biondini, and P. Schmelcher, *Phys. Rev. A* **97**, 043623 (2018).
- [112] T. Busch, and J. R. Anglin, *Phys. Rev. Lett.* **87**, 010401 (2001).
- [113] S. Bandyopadhyay, A. Roy, and D. Angom, *Phys. Rev. A* **96**, 043603, (2017).
- [114] A. S. Dehkharghani, A. G. Volosniev, and N. T. Zinner, *Phys. Rev. Lett.* **121**, 080405 (2018).
- [115] A. Klein, and M. Fleischhauer, *Phys. Rev. A* **71**, 033605 (2005).
- [116] A. Camacho-Guardian, L. P. Ardila, T. Pohl, and G. M. Bruun, *Phys. Rev. Lett.* **121**, 013401 (2018).
- [117] H. Tajima, and S. Uchino, *Phys. Rev. A* **99**, 063606 (2019).
- [118] H. Tajima, and S. Uchino, *New J. Phys.* **20**, 073048 (2018).